



# Doped Mn modulates the local charge distribution of cobalt-based spinel catalysts to promote the availability of ligand lattice oxygen for complete oxidation of methane

Linghe Song<sup>a</sup>, Hang Zhang<sup>a</sup>, Juxia Xiong<sup>a</sup>, Ziyang Chen<sup>a</sup>, Yue Liu<sup>a</sup>, Haitao Zhou<sup>a</sup>, Weixing Yang<sup>a,d</sup>, Dahua Cao<sup>d</sup>, Haomin Huang<sup>a,b,c</sup>, Limin Chen<sup>a,b,c</sup>, Mingli Fu<sup>a,b,c</sup>, Daiqi Ye<sup>a,b,c,\*</sup>

<sup>a</sup> School of Environment and Energy, South China University of Technology, Guangzhou 510006, PR China

<sup>b</sup> Guangdong Provincial Key Laboratory of Atmospheric Environment and Pollution Control, Guangzhou 510006, PR China

<sup>c</sup> Guangdong Provincial Engineering and Technology Research Centre for Environmental Risk Prevention and Emergency Disposal, South China University of Technology, Guangzhou Higher Education Mega Centre, Guangzhou 510006, PR China

<sup>d</sup> Foshan Shunde Midea Electrical Heating Appliances Manufacturing Co., Ltd, Foshan 528300, China

## ARTICLE INFO

### Keywords:

Spinel Co<sub>3</sub>O<sub>4</sub>  
Mn doping  
Methane oxidation  
Lattice oxygen activation  
Local charge distribution

## ABSTRACT

Doping other metals such as Mn, Ni, In, et al. is known as an effective strategy to improve the environmental catalytic performance of Co<sub>3</sub>O<sub>4</sub>. In our works, Mn ions were successfully incorporated into the lattice of Co<sub>3</sub>O<sub>4</sub> via the oxalic acid synchronous complexation method. The Mn ions preferentially occupy octahedrally coordinated Co<sup>3+</sup> sites and constructing the Mn-O-Co structure. In addition, theoretical calculation further verified that the enhanced catalytic performance of Co<sub>5</sub>Mn<sub>1</sub> originated from highly reactive lattice oxygen coordinated with both Mn and Co ions. Significantly, Mn ions transfer more electrons to lattice oxygen. This oxygen sites have the lower oxygen vacancy formation energy ( $E_{\text{Ov}} = 1.94$  eV), allowing the lattice oxygen to participate in the reaction following the MvK mechanism in the high temperature range. Collectively, this work is helpful to understand the mechanism of effect of Mn ion doping on the physical and chemical properties of Co-based catalysts.

## 1. Introduction

Methane in the current global atmosphere is a trace gas, but its increasing anthropogenic emissions will significantly increase methane concentration in the atmosphere. [1] What is noteworthy is that the global warming potential of methane at 20-year levels is 84 times that of carbon dioxide and 28 times that at 100-year levels. [2] In addition, emissions of methane contribute more than 25% to the current global warming, second only to carbon dioxide. Therefore, mitigating methane emissions presents a viable strategy for decelerating the pace of climate change.

The cleavage of the C-H bond in methane is hindered by a high reaction energy barrier, the direct combustion mode without catalyst requires a higher temperature over 1000 °C. Under such conditions, undesirable nitrogen oxides and other secondary pollutants will be produced. [3,4] Therefore, low-temperature catalytic combustion is the effective solution to reduce the harmful impact of low-concentration

methane emissions on the environment. After a deep oxidation process, low-concentration methane is completely oxidized, and the amount of unnecessary nitrogen oxides is reduced.

Compared to precious metals, oxide materials such as spinel and perovskite exhibit equally excellent activity and they are regarded as potential catalysts for methane oxidation. [5] It is noteworthy that cobalt spinel is considered as one of the most promising catalysts, due to the rapid redox cycling between Co<sup>2+</sup> ↔ Co<sup>3+</sup> and enhanced oxygen donating ability, which exhibits good activity for the activation of C-H bonds. [6–8] Spinel Co<sub>3</sub>O<sub>4</sub> consists of Co<sup>2+</sup> sites and Co<sup>3+</sup> sites, with the former coordinated by four adjacent oxygen ions to form a tetrahedron and the latter coordinated by six adjacent oxygen ions to form an octahedron. [9] The adsorption of methane is mainly attributed to the direct interaction of the σ orbitals of the methane molecule on the 3d orbitals of the cobalt cations. The generated \*CH<sub>3</sub> is further oxidized and dehydrogenated to eventually produce CO<sub>2</sub> and H<sub>2</sub>O [10].

The methane oxidation performance of Co<sub>3</sub>O<sub>4</sub> can be improved with

\* Corresponding author at: School of Environment and Energy, South China University of Technology, Guangzhou 510006, PR China.

E-mail address: [cedqye@scut.edu.cn](mailto:cedqye@scut.edu.cn) (D. Ye).

<https://doi.org/10.1016/j.apcatb.2023.123547>

Received 3 August 2023; Received in revised form 5 November 2023; Accepted 20 November 2023

Available online 23 November 2023

0926-3373/© 2023 Elsevier B.V. All rights reserved.

appropriate bulk doping and morphological engineering. By altering the morphological structure and electrical features of the host metal oxide, the metal dopant can influence the adsorption activation capacity of reactants. [11] Especially spinel Co-based oxides ( $\text{Co}_2\text{MO}_4$ , M: transition-metal) the electronic structure of the system can be optimized by modulating the occupancy sites of M cations to achieve improved catalytic activity, which has attracted much attention. The interaction of Co and other metal ions considerably increased the redox performance and catalytic activity for complete oxidation of methane compared to individual metal oxide. [12,13] Mn-doped, Ni-doped cobalt spinel catalysis achieved complete methane oxidation below 350–400 °C due to the synergistic effect between different cations. [14,15] Activation capacity of catalysts for gaseous oxygen and utilization of lattice oxygen varies with the surface structures of  $\text{Co}_3\text{O}_4$  which depend on the exact coordination between metal cations. Although effective catalytic activity of cobalt-based multicomponent composite catalyst systems was reported for a long time, [16,17] there is lack of deep understanding of the relationship between the local electronic modulation of doped elements and catalytic activity.

Herein, Mn ions were successfully incorporated into the lattice of  $\text{Co}_3\text{O}_4$  by the oxalic acid synchronous coupling method. The Mn ions preferentially occupy octahedrally coordinated  $\text{Co}^{3+}$  sites ( $\text{Co}_{\text{Oh}}^{3+}$ ) and constructing asymmetric Mn-O-Co structure. We distinguish between intrinsic oxygen vacancies and induced oxygen vacancies, the former is defined as oxygen vacancies present at room temperature, which have been shown to be widely present in  $\text{Co}_3\text{O}_4$  in numerous studies. [18] The latter is defined as oxygen vacancies created by changes in reaction atmosphere and temperature. Our experiments show that pure  $\text{Co}_3\text{O}_4$  catalyst exhibited good catalytic activity at low temperature due to its abundant intrinsic oxygen vacancies, which induced the direct activation of adsorbed gaseous oxygen. The higher high-temperature activity of the  $\text{Co}_5\text{Mn}_1$  is attributed to the Mn-O-Co structure constructed by Mn substituting. Although Mn doping reduces the content of intrinsic oxygen vacancies, which is not favorable for catalysis in the low-temperature interval, it also increased lattice oxygen activity and reduces the difficulty of induced oxygen vacancy generation of Mn-O-Co sites, enabling induced oxygen vacancies as a major active contributor to the high temperature range. Furthermore, the asymmetric Mn-O<sub>v</sub>-Co sites more tend to adsorb activated gaseous oxygen compared to the  $\text{Co-O}_v\text{-Co}$  sites, thus increasing the catalyst surface oxygen cycling rate.

## 2. EXPERIMENTAL SECTION

### 2.1. Chemical materials

Cobalt acetate tetrahydrate ( $\text{Co}(\text{CH}_3\text{COO})_2 \cdot 4 \text{H}_2\text{O}$ ), manganese acetate tetrahydrate ( $\text{Mn}(\text{CH}_3\text{COO})_2 \cdot 4 \text{H}_2\text{O}$ ), urea, and oxalic acid dihydrate ( $\text{C}_2\text{H}_2\text{O}_4 \cdot 2 \text{H}_2\text{O}$ ) (>99.9%) were purchased from Sigma-Aldrich. All chemicals are of analytical grade purity and can be used without further purification.

### 2.2. Catalyst Preparation

#### 2.2.1. Synthesis of pure $\text{Co}_3\text{O}_4$ and MnOx samples

As shown in Scheme 1, 24 mmol  $\text{Co}(\text{CH}_3\text{COO})_2 \cdot 4 \text{H}_2\text{O}$  and 36 mmol  $\text{C}_2\text{H}_2\text{O}_4 \cdot 2 \text{H}_2\text{O}$  were dissolved in 250 mL distilled water, respectively. The oxalic acid solution was slowly added to the vigorously stirred precursor solution to form a complex and maintained at room temperature (25 °C) for 12 h. The obtained above solution was then centrifuged and washed three times with ethanol and deionized water and being dried in an oven at 80 °C overnight. Finally, the sample was calcined at 500 °C for 3 h. The obtained sample is denoted as pure  $\text{Co}_3\text{O}_4$ . MnOx was prepared in exactly the same method as pure  $\text{Co}_3\text{O}_4$ , with the difference that 24 mmol  $\text{Co}(\text{CH}_3\text{COO})_2 \cdot 4 \text{H}_2\text{O}$  was replaced with 24 mmol  $\text{Mn}(\text{CH}_3\text{COO})_2 \cdot 4 \text{H}_2\text{O}$ .

#### 2.2.2. Synthesis of $\text{Co}_x\text{Mn}_y$ samples

The synthetic procedure of  $\text{Co}_x\text{Mn}_y$  was similar to that of  $\text{Co}_3\text{O}_4$  catalysts through a synthesis strategy of synchronous complexation. Acetate ( $\text{Co}^{2+}/\text{Mn}^{2+} = 20, 10, 5, 2, 0.5$ ) and oxalic acid were dissolved in 250 mL distilled water and kept at room temperature (25 °C) for 12 h. The drying and calcination procedures were the same as for  $\text{Co}_3\text{O}_4$ . The obtained metal oxide product was labeled as  $\text{Co}_{20}\text{Mn}_1$  (when feeding  $\text{Co}^{2+}/\text{Mn}^{2+} = 20$ ),  $\text{Co}_{10}\text{Mn}_1$  ( $\text{Co}^{2+}/\text{Mn}^{2+} = 10$ ),  $\text{Co}_5\text{Mn}_1$  ( $\text{Co}^{2+}/\text{Mn}^{2+} = 5$ ),  $\text{Co}_2\text{Mn}_1$  ( $\text{Co}^{2+}/\text{Mn}^{2+} = 2$ ), and  $\text{Co}_1\text{Mn}_2$  ( $\text{Co}^{2+}/\text{Mn}^{2+} = 0.5$ ).

### 2.3. Catalyst characterization

All the characterization methods of the as-prepared catalysts were implemented via various techniques. All the detailed characterization information are described in the Supplementary Information (SI) file.

### 2.4. Evaluation of catalytic activity

Methane catalytic activity is evaluated by on-line temperature-programmed oxidation. Detailed manipulation procedures can be found in SI file.

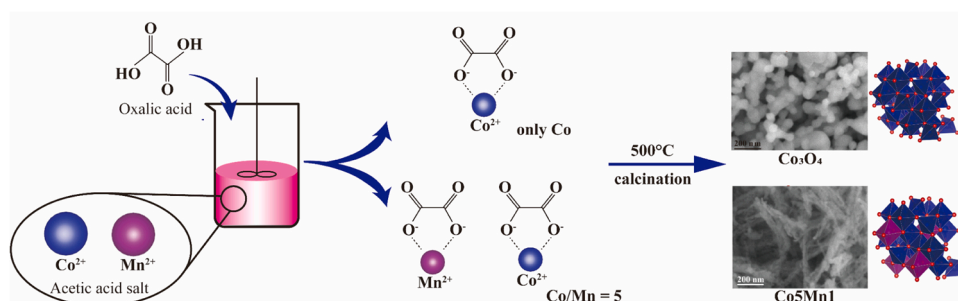
### 2.5. DFT Calculations

DFT calculations were employed to analyze the formation energy of oxygen vacancies, the electronic structure, adsorption energy of oxygen, and methane molecular activation energy over the  $\text{Co}_3\text{O}_4$  {110} and  $\text{Co}_5\text{Mn}_1$  {111}. The detailed calculational methodology can be found in SI file.

## 3. Results and discussion

### 3.1. Structure and texture of catalysts

The X-ray diffraction (XRD) diffractogram of as-prepared pure  $\text{Co}_3\text{O}_4$  and  $\text{Co}_x\text{Mn}_y$  catalysts is demonstrated in Fig. 1a. The patterns indicating that the cubic structure of pure  $\text{Co}_3\text{O}_4$ ,  $\text{Co}_{20}\text{Mn}_1$ ,  $\text{Co}_{10}\text{Mn}_1$ ,  $\text{Co}_5\text{Mn}_1$



**Scheme 1.** Schematic diagram of pure  $\text{Co}_3\text{O}_4$  and Mn-doped  $\text{Co}_3\text{O}_4$  catalysts via facile oxalic acid synchronous complexation method.

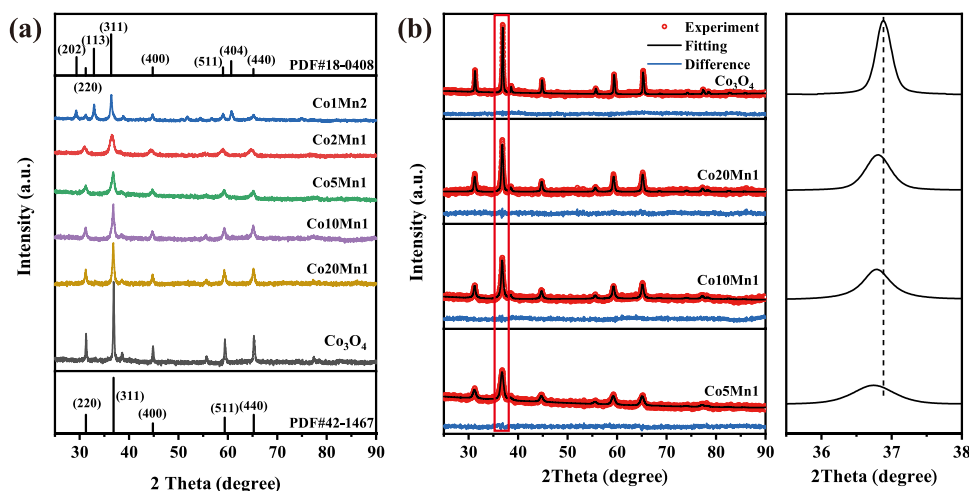


Fig. 1. XRD patterns (a) and Rietveld refinements results (b) of pure  $\text{Co}_3\text{O}_4$  and  $\text{Co}_x\text{Mn}_y$  catalysts.

and  $\text{Co}_2\text{Mn}_1$  corresponding to  $\text{Co}_3\text{O}_4$  spinel network (space group:  $Fd\bar{3}m$  (227), PDF #42–1467), the crystalline feature is not disturbed by adding a certain amount of manganese. [19] However, the main diffraction patterns of  $\text{Co}_1\text{Mn}_2$  belong to cobalt manganese oxide (PDF #18–0408), completely different crystal phase than other catalysts. No distinct diffraction peaks corresponding to pure  $\text{MnO}_x$  were observed in the XRD patterns, indicating that no agglomeration of Mn species occurred for all samples. To observe the precision effect of Mn substitution on the crystal phase, the average crystallite sizes of  $\text{Co}_3\text{O}_4$  and  $\text{Co}_x\text{Mn}_y$  oxides were determined using the Scherrer equation based on XRD results, and are presented in Table 1.

The crystallite size decreased significantly from 47.5 nm (pure  $\text{Co}_3\text{O}_4$ ) to 9.8 nm ( $\text{Co}_2\text{Mn}_1$ ) with the increase of Mn ions substitution, the presence of Mn ions during synchronous complexation is likely to affect the nucleation and growth rate of crystallite, which could explain the observed phenomenon. [20] Fig. 1b illustrates the Rietveld refinements results for pure  $\text{Co}_3\text{O}_4$ ,  $\text{Co}_{20}\text{Mn}_1$ ,  $\text{Co}_{10}\text{Mn}_1$ , and  $\text{Co}_5\text{Mn}_1$ , Table 1 summarizes the room-temperature unit-cell parameters. Obviously, lattice constant gradually increases, and the strongest characteristic peak assigned to (311) planes shift towards lower angle with the increase of Mn substitution. Although there are differences in the radii of  $\text{Co}^{3+}$  (0.61 Å) and  $\text{Mn}^{3+}$  (0.65 Å) before and after doping, the Jahn-Teller effect present in doped Mn may be the main cause of lattice distortion [15,21].

To explore the substitution site and verify its influence on the structure, Co ions with different coordination environments in the primitive cell were substituted with Mn ions and performed geometry optimization to obtain the lowest energy steady state adopting the theoretical calculation method. [14] Table S1 demonstrates four different substitution models of crystals tested in our calculations,

substituting a  $\text{Co}_{\text{Th}}^{2+}$  at a different site with an  $\text{Mn}_{\text{Th}}^{2+}$  (Table S1, type I and II) and substituting a  $\text{Co}_{\text{Oh}}^{3+}$  with a  $\text{Mn}_{\text{Oh}}^{3+}$ , respectively (Table S1, type III and IV). Theoretical calculations reveal that the type III and IV crystal structures have lower system energy, which means they are more stable. From the energy perspective, it is proved that Mn ions are more likely to substitute the  $\text{Co}_{\text{Oh}}^{3+}$  instead of  $\text{Co}_{\text{Th}}^{2+}$ , which is coincides with the point that the absolute octahedral site preference energies from the literature [22] are in the order  $\text{Mn}^{3+}/\text{Mn}^{4+} > \text{Co}^{3+} > \text{Co}^{2+}$ . The following calculations considered the idealized model with Mn ions substituting the  $\text{Co}_{\text{Oh}}^{3+}$ .

Based on the substitution rule of Mn ions in the cobalt-based spinel lattice in the previous section, the ideal substitution model shown in Fig. 2a is proposed. Clearly, the Mn ions in  $\text{Co}_{20}\text{Mn}_1$ ,  $\text{Co}_{10}\text{Mn}_1$  and  $\text{Co}_5\text{Mn}_1$  catalysts substitute a single  $\text{Co}_{\text{Oh}}^{3+}$  site in the primitive cell, and the ratio of Mn-O-Co structure in bulk increases with the Mn content, and the largest ratio of Mn-O-Co structure when  $\text{Co}/\text{Mn} = 5$  ( $\text{Co}_5\text{Mn}_1$  model). In the  $\text{Co}_2\text{Mn}_1$  model, the Mn ions all substitute two  $\text{Co}_{\text{Oh}}^{3+}$  sites in a single primitive cell so that the adjacent Mn ions are bonded to each other by O ions and constitute the Mn-O-Mn structure. Due to the change in the crystal structure of the  $\text{Co}_1\text{Mn}_2$  catalyst according to the XRD results, the primitive cell model of  $\text{Co}_1\text{Mn}_2$  is shown in Fig. 2a, where all the Mn ions occupy octahedral sites and the Co ions occupy tetrahedral sites. The local structure of the prepared pure  $\text{Co}_3\text{O}_4$  catalyst and the lattice distortion of the Mn-substituted  $\text{Co}_3\text{O}_4$  catalysts were further investigated by Raman spectroscopy as shown in Fig. 2b, the factor group analysis predicts five Raman-active  $A_{1g}$ ,  $F_{2g}^3$ ,  $F_{2g}^2$ ,  $E_g$ , and  $F_{2g}^1$  bands. The band assigned to  $A_{1g}$  symmetry at  $672\text{ cm}^{-1}$  is characteristically ascribed to the octahedral coordination sites ( $\text{CoO}_6$ ), and the band assigned to  $F_{2g}^3$  symmetry at  $188\text{ cm}^{-1}$  is characteristically ascribed to the tetrahedral coordination sites ( $\text{CoO}_4$ ). Raman bands with

Table 1  
Physical and chemical properties and structural parameters of  $\text{Co}_3\text{O}_4$  and Mn doped catalysts.

Samples	<sup>a</sup> Crystallite size / nm	<sup>b</sup> Lattice constant a / Å	<sup>b</sup> Lattice constant b / Å	<sup>b</sup> Lattice constant c / Å	<sup>c</sup> BET SSA / $\text{m}^2\text{ g}^{-1}$	<sup>d</sup> Surface ratio of Co/Mn / %
$\text{Co}_3\text{O}_4$	47.5	8.08458	8.08458	8.08458	34	N/A
$\text{Co}_{20}\text{Mn}_1$	25	8.09626	8.09626	8.09626	52	10.47
$\text{Co}_{10}\text{Mn}_1$	19.9	8.10382	8.10382	8.10382	71	6.04
$\text{Co}_5\text{Mn}_1$	13.3	8.10231	8.10231	8.10231	102	4.92
$\text{Co}_2\text{Mn}_1$	9.8	8.13606	8.13606	8.13606	113	1.20
$\text{Co}_1\text{Mn}_2$	29.9	8.09754	8.09754	9.27033	84	0.45

<sup>a</sup> Average crystallite size is calculated by the Scherrer equation.

<sup>b</sup> Lattice constant refined by the Rietveld method.

<sup>c</sup> Specific surface area obtained by BET method.

<sup>d</sup> Surface atomic ratio of Co/Mn obtained by X-ray photoelectron spectroscopy (XPS)

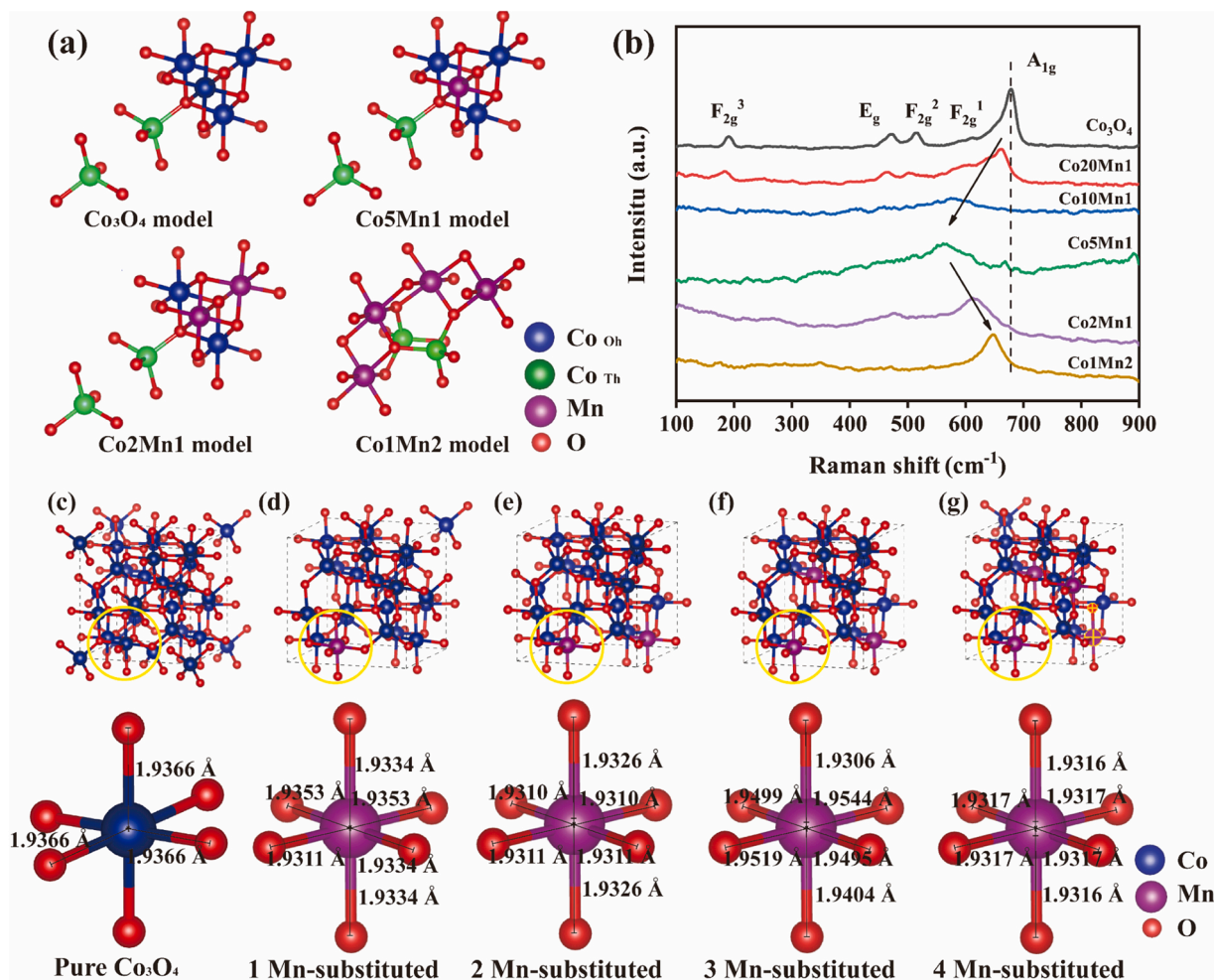


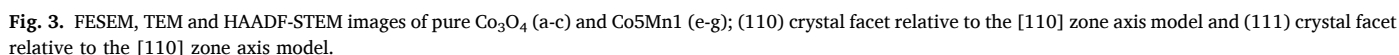
**Fig. 2.** Primitive cells of Co<sub>3</sub>O<sub>4</sub>, Co<sub>5</sub>Mn<sub>1</sub>, Co<sub>2</sub>Mn<sub>1</sub>, and Co<sub>1</sub>Mn<sub>2</sub> catalysts models (a), Raman spectra of pure Co<sub>3</sub>O<sub>4</sub> and Co<sub>x</sub>Mn<sub>y</sub> catalysts (b), and optimized standard Co<sub>3</sub>O<sub>4</sub> crystals cell and Co<sub>x</sub>Mn<sub>y</sub> crystals cell with different Mn substitution amounts (c-g).

medium strength located at 466 and 510 cm<sup>-1</sup> represent E<sub>g</sub> and F<sub>2g</sub><sup>2</sup> symmetry, and the weak band located at 605 cm<sup>-1</sup> represents F<sub>2g</sub><sup>1</sup> symmetry. [23] The peak Raman features are verified according to the coordination of the above model shown in Fig. 2a. For Co<sub>20</sub>Mn<sub>1</sub>, Co<sub>10</sub>Mn<sub>1</sub> and Co<sub>5</sub>Mn<sub>1</sub>, with the increase of Mn substitution, there was a significant red shift in the peak location of A<sub>1g</sub>, indicating successful incorporation of Mn resulting in lattice distortion. [24] The strong Jahn-Teller effect of doped Mn ions in the lattice causes local structural distortions, leading to a shift of the A<sub>1g</sub> peak. [21] The lattice distortion due to Mn doping was further confirmed by calculating the bond lengths of Co(Mn)-O in MnO<sub>6</sub> octahedra by DFT method. We constructed standard Co<sub>3</sub>O<sub>4</sub> crystals cell with low concentration of substitution amounts (Co/Mn ≥ 5) and optimized the structure (Fig. 2c-g). According to the method reported by Shannon, this distortion from the ideal symmetric octahedron can be quantified by the variance of Co (Mn) -O bond length. [25,26] As shown in Table S2, the 3 Mn-substituted model in which Mn ions substituted three Co<sup>3+</sup> exhibits the maximum Mn-O bond length variance among all Co<sub>x</sub>Mn<sub>y</sub> samples, demonstrating its highest octahedral distortion, consistent with the low Raman response of Co<sub>10</sub>Mn<sub>1</sub> catalysts due to their similar Mn ion substitution content. Since Mn ions tend to be uniformly dispersed in the lattice, the 4 Mn-substituted model equivalent to the original cell of Co<sub>5</sub>Mn<sub>1</sub> (Co/Mn = 5) will show a higher percentage of octahedral distortion. It implies that the presence of an adequate Mn-O-Co structure for the Co<sub>5</sub>Mn<sub>1</sub> catalyst. The lattice disorder of the system is influenced by the degree of distortion and distortion content. The distorted MnO<sub>6</sub> octahedra are expected to

activate the lattice oxygen of Co<sub>x</sub>Mn<sub>y</sub> oxide to improve the mobility of bulk phase oxygen and reactivity of surface oxygen. [13] In addition, when there is an excess of Mn ions in the system (Co/Mn < 5), primitive cell change from Co<sub>5</sub>Mn<sub>1</sub> to Co<sub>2</sub>Mn<sub>1</sub> and Co<sub>1</sub>Mn<sub>2</sub> model (Fig. 2a), and the system tends to be ordered due to the increase of the symmetric Mn-O-Mn structure, so A<sub>1g</sub> peaks of Co<sub>2</sub>Mn<sub>1</sub> and Co<sub>1</sub>Mn<sub>2</sub> appear again at around 650 cm<sup>-1</sup> which is assigned to be the stretching modes of Mn-O in MnO<sub>6</sub> octahedra [27,28].

The SEM images reveal morphologies of different proportions Mn-substituted Co<sub>3</sub>O<sub>4</sub> catalyst. As shown in Fig. 3, pure Co<sub>3</sub>O<sub>4</sub> catalysts are composed of nanoparticles with different sizes. When an appropriate amount of Mn ions was added (for the Co<sub>5</sub>Mn<sub>1</sub> catalyst), the nanoparticles self-assemble into a rod-like structure, possibly due to the substituting of Mn, which restricts the growth of the dominant crystal planes. Fig. 3c1, c2 and c3 demonstrate HAADF-STEM images of Co<sub>3</sub>O<sub>4</sub>, with the highlight being the response of Co ions. Due to the lower atomic number of oxygen, the projection potential is smaller and oxygen atoms are almost absent in the HAADF-STEM imaging. In addition, we attribute Co ions in the images based on the standard crystal cell model along the [110] zone axis. The red circles are octahedrally coordinated Co (oct-Co) and the yellow orbs are tetrahedrally coordinated Co (tetra-Co). As can be seen in the Fig. 3c1, c2 and c3, the different locations we randomly selected all expose mainly (110) crystalline facets, and the different (110) crystalline facets are connected to each other by high-index crystalline steps. Fig. 3c4 shows a localized enlarged Co<sub>3</sub>O<sub>4</sub> particle boundary, and the exposed surface atoms can be well matched with





### 3.2. Catalytic performance

oxidation process. Each sample was repeated five times to take the average value to ensure the reliability of the experimental results, and the experimental errors have been marked in the figure. Using T<sub>90</sub> (90% conversions of CH<sub>4</sub>) as the activity criterion for comparison, the activities of this series of catalysts were in the order of Co<sub>5</sub>Mn<sub>1</sub> > Co<sub>2</sub>Mn<sub>1</sub> > pure Co<sub>3</sub>O<sub>4</sub> ≈ Co<sub>1</sub>Mn<sub>2</sub> > MnOx. More prominently, the Co<sub>5</sub>Mn<sub>1</sub> catalyst exhibits the most outstanding catalytic activity with 90% CH<sub>4</sub> conversion at 367 °C, which is 47 °C lower than Co<sub>3</sub>O<sub>4</sub>. The MnOx catalyst exhibited much weaker methane catalytic activity compared to the other catalysts, which further demonstrated the synergistic effect of Mn and Co in Mn-doped Co<sub>3</sub>O<sub>4</sub> catalysts. At the same time, Co<sub>5</sub>Mn<sub>1</sub> catalysts do not promote methane oxidation over the entire temperature range. As shown in Fig. 4b, Co<sub>3</sub>O<sub>4</sub> samples with spinel crystalline phase have much better catalytic activity than Co<sub>5</sub>Mn<sub>1</sub> catalysts in the low-temperature range (< 290 °C). And the substituting of the appropriate amount of Mn showed a significant promotion effect on the cobalt-based catalysts at high temperatures (> 290 °C). It is suggested that Mn ions produce synergistic effects with Co

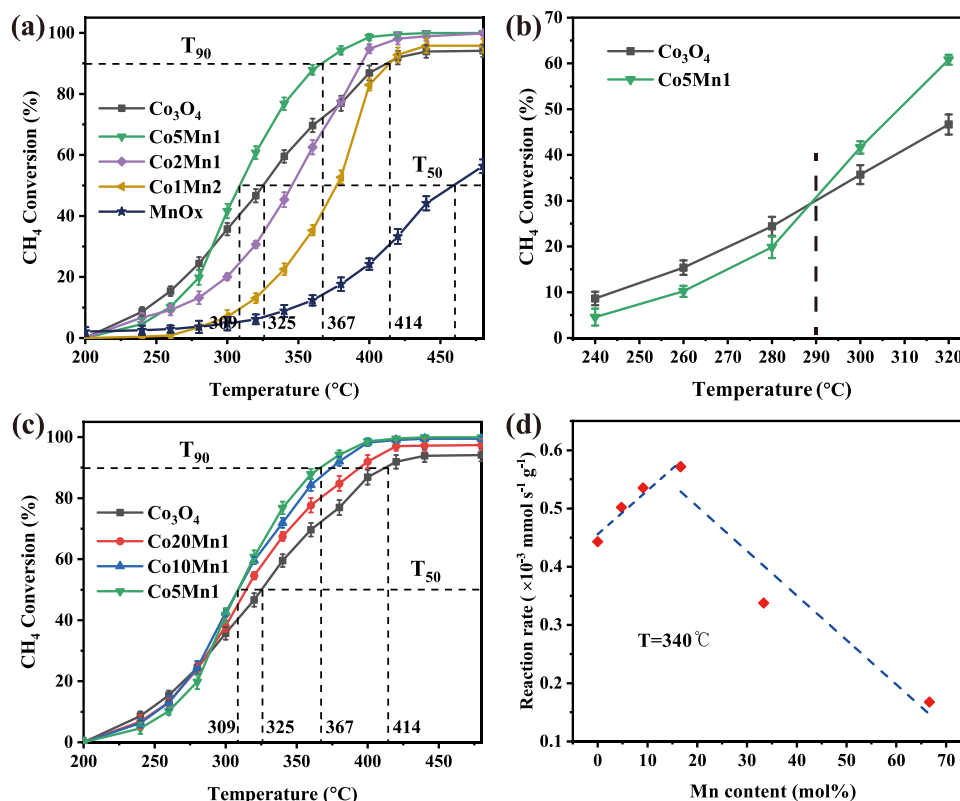


**Fig. 4.** Light-off curves for CH<sub>4</sub> conversion over pure Co<sub>3</sub>O<sub>4</sub>, Co<sub>5</sub>Mn<sub>1</sub>, Co<sub>2</sub>Mn<sub>1</sub>, Co<sub>1</sub>Mn<sub>2</sub> and MnOx catalysts (a), Comparison of methane conversion between Co<sub>5</sub>Mn<sub>1</sub> and Co<sub>3</sub>O<sub>4</sub> catalysts at low temperatures (b), light-off curves for CH<sub>4</sub> conversion over pure Co<sub>3</sub>O<sub>4</sub>, Co<sub>20</sub>Mn<sub>1</sub>, Co<sub>10</sub>Mn<sub>1</sub> and Co<sub>5</sub>Mn<sub>1</sub> catalysts (c), and the trend of conversion rate with the increase of Mn ions in Co<sub>x</sub>Mn<sub>y</sub> catalysts. (d). Gas mixture: 1% CH<sub>4</sub>, 20% O<sub>2</sub>, N<sub>2</sub> as balance gas, GHSV = 60,000 mL/(g·h).

ions by constructing Mn-O-Co structures at high temperatures, while the synergistic effects at low temperatures are not noticeable.

The structural analysis showed that the Mn-O-Co structure in the system reached the maximum content at Co/Mn = 5. To further prove that Mn-O-Co structure may be the origin of methane catalytic activity, gradually increasing the substituted amount of Mn in Cobalt-based catalyst, Co<sub>20</sub>Mn<sub>1</sub> and Co<sub>10</sub>Mn<sub>1</sub> were evaluated to prove the relationship between catalytic activity and content of Mn-O-Co structure. As shown in Fig. 4c, in the high-temperature range (>290 °C), the catalytic activity of Co<sub>20</sub>Mn<sub>1</sub> and Co<sub>10</sub>Mn<sub>1</sub> is higher than that of pure Co<sub>3</sub>O<sub>4</sub> but slightly lower than that of Co<sub>5</sub>Mn<sub>1</sub> and perfectly consistent with the expected results that catalytic activity of methane be better with the increase of Mn-O-Co structure content. Fig. 4d demonstrates the trend of catalytic rate with Mn-substituted content at 340 °C. When Co/Mn > 5, the catalytic activity for methane increases with the increase of Mn-substituted content. The reaction rate of Co<sub>5</sub>Mn<sub>1</sub> catalyst was significantly higher by about 30% compared to Co<sub>3</sub>O<sub>4</sub>. For Co<sub>2</sub>Mn<sub>1</sub> and Co<sub>1</sub>Mn<sub>2</sub>, the reaction rate showed a negative correlation with the increase of Mn content. It is noteworthy that the methane catalytic activity of Co<sub>1</sub>Mn<sub>2</sub> is even significantly lower than that of the pure Co<sub>3</sub>O<sub>4</sub> catalyst. Therefore, excessive Mn ions are not conducive to methane catalytic activity, which may be due to the construction of an excess Mn-O-Mn structure as showed in Fig. 2a Co<sub>1</sub>Mn<sub>2</sub> model. For this significant difference in catalytic performance, we excluded the interference of transport and diffusion factors by turnover frequency (TOF) calculations. TOF is calculated based on the active site and reaction rate (Table S3). CO chemisorption experiments (Fig. S2) were used to titrate the surface metal atoms of the catalysts to determine the number of active sites. These experiments reveal that the exposed active sites decrease with Mn doping. Interestingly, the Co<sub>5</sub>Mn<sub>1</sub> catalyst exhibited the best intrinsic catalytic activity.

We list the previously reported methane catalytic properties of Co-

based catalysts in Table S4, the catalytic activity of Co<sub>5</sub>Mn<sub>1</sub> is comparable or even better than most of the reported Co-based or some noble metal catalysts. Next, the thermal stability of the Co<sub>5</sub>Mn<sub>1</sub> catalysts were evaluated at 310 °C and 400 °C for 72 h (Fig. S3). The methane conversion to rate over Co<sub>5</sub>Mn<sub>1</sub> catalysts is steadily maintained about 100% at 400 °C and 50% at 310 °C. This result indicates that the Co<sub>5</sub>Mn<sub>1</sub> catalysts has excellent long-term thermal stability. There was a little difference between CO<sub>2</sub> yield (Fig. S4) and methane conversion rate, and no incomplete oxidation products were detected, as substantiated by the good carbon balance (>98.5%) in all the catalytic tests carried out in presence of the gas mixture containing 1% CH<sub>4</sub> + 20% O<sub>2</sub> balanced in N<sub>2</sub>. Fig. S5 illustrates five consecutive runs curves of methane combustion over Co<sub>5</sub>Mn<sub>1</sub> catalysts. It can be seen that the conversion of the other run curve decreases slightly (< 5%) compared with the fresh sample. As shown in Fig. S6, the XRD spectra before and after the reaction proved the stability of the catalyst structure.

### 3.3. Chemical states of catalysts

Hydrogen temperature-programmed reduction (H<sub>2</sub>-TPR) experiment was employed to investigate the reduction properties of Co species and Mn species are demonstrated in Fig. S7a. For the Co<sub>3</sub>O<sub>4</sub> catalyst, the reduction peak at 289 °C corresponds to the reduction of Co<sup>3+</sup> to Co<sup>2+</sup>, and the peak at 350–550 °C corresponds to Co<sup>2+</sup> to metallic Co. [29] For the Co<sub>5</sub>Mn<sub>1</sub> catalyst, it is observed that weak reduction peaks at about 209 °C can be attributed to the reduction of Mn<sup>4+</sup> to Mn<sup>3+</sup>. [30] The reduction of Mn<sup>4+</sup> is extremely sensitive in reducing atmosphere. For the Co<sub>1</sub>Mn<sub>2</sub> catalyst, the peak area at around 209 °C is similar to Co<sub>5</sub>Mn<sub>1</sub> according to the peak fitting result (Table S5), indicating that the Mn ion increased in Co<sub>2</sub>Mn<sub>1</sub> than Co<sub>5</sub>Mn<sub>1</sub> does not exhibit a high valence state in the system, this means that the number of sites in the system that can provide high valence Mn has occupied reaches the

maximum in Co5Mn1. In addition, the reduction properties in the temperature range of 50–150 °C are closely related to the adsorption properties of oxygen species. The reduction peak of pure Co<sub>3</sub>O<sub>4</sub> at 76 °C is attributed to the reduction of adsorbed oxygen species (O<sub>2</sub>, O<sub>2</sub><sup>-</sup>, or O<sup>-</sup>), [31] and the temperature is significantly lower than that of Co5Mn1 and Co1Mn2 catalysts. It indicates that pure Co<sub>3</sub>O<sub>4</sub> catalyst are more likely to stabilize the adsorbed oxygen species, which was further verified by subsequent EPR and XPS experiments.

Extensive research has been conducted to demonstrate the actual presence of oxygen vacancies on the surface of pure Co<sub>3</sub>O<sub>4</sub> at low temperatures. Herein, intrinsic oxygen vacancy content of the catalyst is verified by electron paramagnetic resonance (EPR) measurement because the unpaired electrons at the oxygen vacancy produce a distinct EPR response. The experiments were pretreated with 20%O<sub>2</sub>/N<sub>2</sub> at 300 °C to remove the interference of residual carbon impurity. The intensity of the symmetrical peak at a g value of 2.003 is directly related to the oxygen vacancy concentration.[32] As shown in Fig. S7b, the substitution of Mn results in a significant decrease in the intensity of the symmetric peak, indicating that the Mn substitution can decrease the

concentration of intrinsic oxygen vacancies. This may be because Mn ions exhibit a high valence state (Mn<sup>3+</sup> and Mn<sup>4+</sup>), since one Co<sup>3+</sup> requires one and a half O<sub>2</sub><sup>2-</sup> equilibrium charges, while one Mn<sup>4+</sup> requires two O<sub>2</sub><sup>2-</sup> equilibrium charges. So Co5Mn1 require more lattice oxygen ions to balance the charge.

The changes in the surface composition and chemical state of the CoxMny catalysts with increasing Mn content were investigated using X-ray photoelectron spectroscopy (XPS). The spectra recorded and fitted in the Co 2p, Mn 3s, Mn 2p, and O 1s regions are shown in Fig. 5. For Co20Mn1, Co10Mn1, and Co5Mn1, the main peak of Co 2p<sup>3/2</sup> has a slight shift of about 0.5 eV compared to pure Co<sub>3</sub>O<sub>4</sub>, suggesting that the interaction between Mn and Co atoms modulates the electronic state of Co.[33] The decrease in Co valence state due to Mn doping is also verified by Bader charge calculations, where the average Bader charge in Co<sub>3</sub>O<sub>4</sub> is 1.26 eV slightly higher than that of Co5Mn1 at 1.10 eV (Table S6). The shakeup satellites peak at 785.9 eV are more and more apparent with the increase of Mn substitution, especially for Co1Mn2 and Co2Mn1 samples.[34] It can be seen as a sign of Co<sup>3+</sup> reduced because Mn ions occupy the Co<sup>3+</sup> site. In Fig. S8a, the binding energy

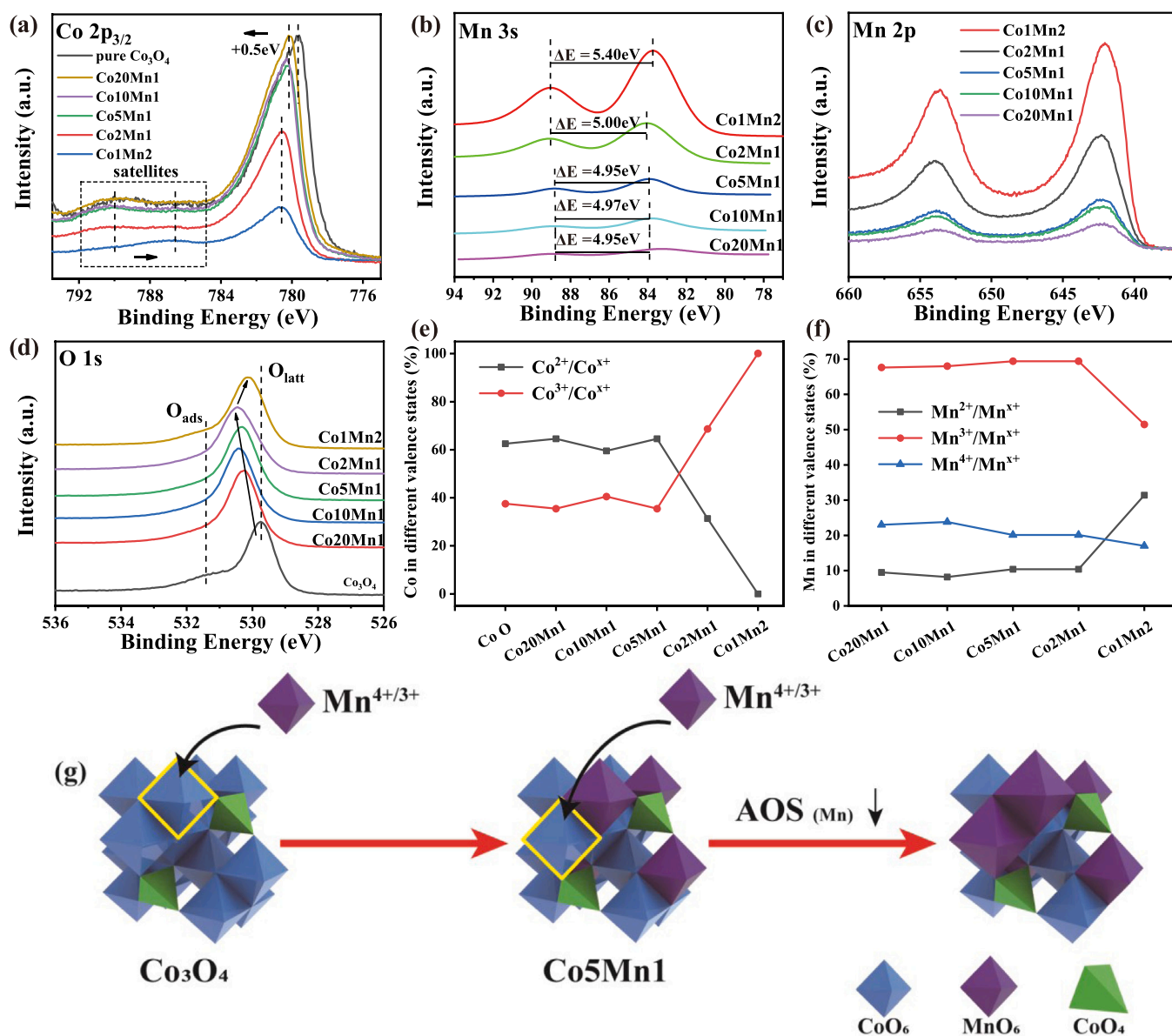


Fig. 5. High-resolution XPS spectra of Co 2p (a), Mn 2s (b), Mn 3p (c) and O 1s (d); the content of Co ions in different valence states based on Co2p peak fitting (e) and the content of Mn ions in different valence states based on Mn 2p peak fitting (f); schematic diagram of Mn substitution (g).



peak at around 779.8, 779.1, and 782.2 eV corresponds to  $\text{Co}^{3+}$  in octahedral sites, mixed Co (II, III) and  $\text{Co}^{2+}$  in tetrahedral sites, respectively.[20] The atomic ratio of  $\text{Co}^{3+}$  and  $\text{Co}^{2+}$  can be calculated from the area ratio of the fitting date. The detailed results are summarized in Table 2, and the change tendency is illustrated in Fig. 5e. Clearly, when  $\text{Co}/\text{Mn} \geq 5$ , there is no significant reduction of  $\text{Co}^{3+}$ . However, the  $\text{Co}^{3+}/(\text{Co}^{3+}+\text{Co}^{2+})$  ratio of Co2Mn1 significantly lower than the pure  $\text{Co}_3\text{O}_4$  catalyst (0.3 vs. 0.6), probably because Mn ions occupied half of the  $\text{Co}^{3+}$  site. For the Co1Mn2 sample, the Co ion is present in the state of  $\text{Co}^{2+}$ , which further verified that the octahedrally coordinated  $\text{Co}^{3+}$  is substituted mainly by Mn ions which corresponds to the model of Co1Mn2.

Fig. 5b show the high-resolution XPS spectra in the Mn 3s region. The average oxidation state (AOS) of Mn in different samples of  $\text{Co}_x\text{Mn}_y$  catalysts was calculated according to the magnitude of the Mn 3s multiplet splitting energy by the following equation, and the result is listed in Table 2.[35,36].

$$\text{AOS} = 8.95 - 1.13\Delta E_s (\text{eV})$$

where  $\Delta E_s$  denotes the multiplet splitting energy, i.e., the energy difference between the  $\text{Mn}2p_{1/2}$  peak and  $\text{Mn}2p_{3/2}$ .

Clearly, Co20Mn1, Co10Mn1, Co5Mn1 and Co2Mn1 have similar AOS of about 3.3 which are all greater than 2.85 for Co1Mn2. As shown in Table 2, the AOS values of the  $\text{Co}_x\text{Mn}_y$  catalysts gradually decreased with the increase of Mn, the average valence of the high Co/Mn samples (Co5Mn1, Co10Mn1, Co20Mn1) were similar and all-around +3.3. It shows that the appropriate amount of Mn ion exists stably in the high valence state ( $\text{Mn}^{3+}$  or  $\text{Mn}^{4+}$ ). Moreover, the presence of the Mn species ( $\text{Mn}^{3+}$  or  $\text{Mn}^{4+}$ ) agrees with the  $\text{H}_2$  consumption peaks in the TPR results at 209 °C. However, the Co1Mn2 catalyst had the smallest AOS value, which indicates that excessive Mn ions lead to a decrease in the chemistry valence, probably due to the substitute of  $\text{Co}^{3+}$  or  $\text{Co}^{2+}$  by the excess Mn in the lower valence state ( $\text{Mn}^{2+}$  or  $\text{Mn}^{3+}$ ) or constructed Mn-O-Mn structure, which is also consistent with the results of  $\text{H}_2$ -TPR.

To further investigate the different presence of valence states of surface Mn, the XPS spectra of Mn 2p of pure  $\text{Co}_3\text{O}_4$  and  $\text{Co}_x\text{Mn}_y$  catalysts are shown in Fig. 5c and fitting analysis results are shown in Fig. S8b, the Mn 2p spectra were deconvoluted into three components,  $\text{Mn}^{2+}$ ,  $\text{Mn}^{3+}$  and  $\text{Mn}^{4+}$  at 641.3 eV, 642.8 eV, and 644.6 eV, respectively. Therefore, the exact content of Mn ions in different valence states on the surface is shown in Table 2. The higher valence Mn ions ( $\text{Mn}^{3+}$  and  $\text{Mn}^{4+}$ ) are considered the active sites for cobalt-based catalysts due to their excellent response to methane oxidation.[37] Therefore, it is important to focus on the percentage of  $\text{Mn}^{4+}$  or  $\text{Mn}^{3+}$  in the catalyst. Fig. 5f illustrates the results of the Mn ion valence change based on the Mn2p spectra. The  $\text{Mn}^{4+}$  or  $\text{Mn}^{3+}$  percentage gradually decreases with increasing Mn doping, especially, the  $\text{Mn}^{4+}$  share in Co1Mn2 (17%) is much lower than in the other catalysts. This is due to the change in the coordination environment around the Mn ion caused by different Mn substitution amounts. Combining with the structure analysis, it is found that the Mn-O-Co structure is formed by the direct interaction between the right amount of Mn ions and Co ions at low concentration substituting, the asymmetric structure effectively maintains Mn in a high valence state ( $\text{Mn}^{4+}$ ). However, an excess of Mn ions would occupy

the  $\text{Co}^{3+}$  site to form the Mn-O-Mn structure for Co1Mn2, and the symmetrical local structure causes a decrease in the average oxidation state, which implies a difference in electron transfer between ions (Fig. 5g).

The change of coordination environment affects the binding energy of O 1s. The O 1s XPS spectra and detailed fitting results of pure  $\text{Co}_3\text{O}_4$  and different Mn-substituted  $\text{Co}_3\text{O}_4$  catalysts are shown in Fig. 5d and S8c, respectively. The two peaks corresponding to the surface lattice oxygen species ( $\text{O}_{\text{latt}} = 530.1$  eV) and the surface adsorbed oxygen species ( $\text{O}_{\text{ads}} = 531.6$  eV) can be distinguished through deconvolution.[5,38] As shown in Fig. 5d, the binding energy of  $\text{O}_{\text{latt}}$  is significantly shifted towards the high binding energy with the increase of Mn-substituted content, which was attributed to the fact that the change in the coordination environment of the surface lattice oxygen. The main peak of O 1s of Co1Mn2 catalyst is shifted towards lower binding energy compared to Co5Mn1, which we believe is due to the transformation of Mn-O-Co structure to Mn-O-Mn structure. Since  $\text{O}_{\text{ads}}$  are usually origin from gaseous oxygen adsorbed on oxygen vacancies ( $\text{O}_v$ ), the ratio of  $\text{O}_{\text{ads}}/(\text{O}_{\text{latt}}+\text{O}_{\text{ads}})$  can be used as an indication of the relative content of oxygen vacancies.[39] The peak area ratio of  $\text{O}_{\text{ads}}/(\text{O}_{\text{latt}}+\text{O}_{\text{ads}})$  in the Co5Mn1 catalyst was significantly lower at 21.4% than that of  $\text{O}_{\text{ads}}/(\text{O}_{\text{latt}}+\text{O}_{\text{ads}})$  in the pure  $\text{Co}_3\text{O}_4$  catalyst at 52.2%, and the relative content of oxygen species is shown in Table 2. This means that the substitution behavior of Mn degrades the intrinsic oxygen vacancy content instead, which agrees well with the  $\text{H}_2$ -TPR and EPR. The trend of  $\text{O}_{\text{ads}}/(\text{O}_{\text{latt}}+\text{O}_{\text{ads}})$  versus catalytic activity with the amount of Mn substitution was considered as shown in Fig. 6. There is a positive correlation between intrinsic oxygen vacancy concentration and low temperature catalytic activity, while there is a positive correlation with high temperature catalytic activity and Co/Mn. Therefore, abundant intrinsic oxygen vacancy may be the reason for the excellent methane catalytic activity of  $\text{Co}_3\text{O}_4$  at low temperatures (<290 °C), while the surface lattice oxygen coordinated with Co and Mn species (Mn-O-Co structure) may play a major role at high temperatures (>290 °C).

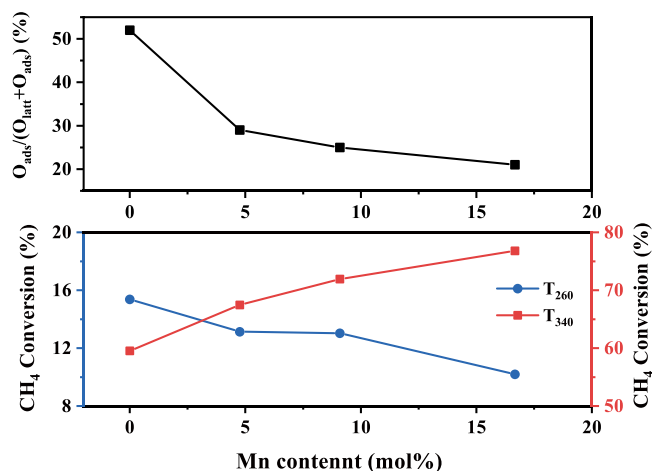


Fig. 6. Relationship between  $\text{O}_{\text{ads}}/(\text{O}_{\text{latt}}+\text{O}_{\text{ads}})$  and low-temperature (260 °C) and high-temperature (340 °C) catalytic activity.

Table 2

Surface chemical composition of pure  $\text{Co}_3\text{O}_4$  and  $\text{Co}_x\text{Mn}_y$  catalysts.

Samples	Mn3s $\Delta E_s$ /eV	AOS	$\text{Mn}^{2+}/\text{Mn}^{3+}$ /%	$\text{Mn}^{3+}/\text{Mn}^{4+}$ /%	$\text{Mn}^{4+}/\text{Mn}^{3+}$ /%	$\text{Co}^{3+}/(\text{Co}^{3+}+\text{Co}^{2+})$ /%	$\text{O}_{\text{ads}}/(\text{O}_{\text{latt}}+\text{O}_{\text{ads}})$ /%
$\text{Co}_3\text{O}_4$	N/A	N/A	N/A	N/A	N/A	65.6	52.2
Co20Mn1	4.95	3.36	9.5	67.6	23.0	65.1	29.4
Co10Mn1	4.97	3.33	8.2	68.0	23.8	63.2	25.1
Co5Mn1	4.95	3.36	10.4	69.4	20.1	60.4	21.4
Co2Mn1	5.00	3.3	10.8	69.2	19.9	31.1	24.3
Co1Mn2	5.40	2.85	31.4	51.5	17.0	0	29.8



### 3.4. Mechanistic analysis of activity

In situ Diffuse reflectance infrared spectroscopy (in situ DRIFTS) investigated the change of intermediate species in the methane oxidation process. As shown in Fig. 7, vibrational peaks attributed to C-H bonds at 1304 and 1344  $\text{cm}^{-1}$  were observed in all catalysts after introducing reactant gases (1%  $\text{CH}_4$  balanced in 20% $\text{O}_2/\text{N}_2$ ) at 30–450  $^{\circ}\text{C}$ . Referred to the literature,[40] vibrational signature at 1450–1600  $\text{cm}^{-1}$  contributed by formate (\*OCHO) and carboxylate (\*COO) appear during the reaction, indicating that the potential reaction path is  $\text{CH}_4 \rightarrow ^*\text{CH}_3 \rightarrow \text{OCHO} \rightarrow \text{OCOO} \rightarrow \text{CO}_2$ .

As shown in Figs. 7a and 7b, the characteristic peak of the key intermediate species appears at 150  $^{\circ}\text{C}$  for the  $\text{Co}_3\text{O}_4$  sample, while for the  $\text{Co}_5\text{Mn}_1$  catalyst, the temperature at which the methane starts to be converted is significantly higher than that for the  $\text{Co}_3\text{O}_4$  catalyst, which suggests that the  $\text{Co}_3\text{O}_4$  catalyst is more capable of activating methane at low temperatures. We normalized the data in Figs. 7a and 7b to determine more clearly the transformation of intermediate species on different catalyst surfaces (Fig. S9). The results indicate that the characteristic peak of the key intermediate species for the  $\text{Co}_3\text{O}_4$  catalyst reaches its maximum at 250  $^{\circ}\text{C}$ , but for the  $\text{Co}_5\text{Mn}_1$  catalyst the conversion reached a maximum at 200  $^{\circ}\text{C}$ , and the characteristic peaks at 1450–1600  $\text{cm}^{-1}$  decreased rapidly with further increase in temperature, which indicated that the  $\text{Co}_5\text{Mn}_1$  catalyst was able to significantly promote the rapid conversion of the intermediate species.

In order to further investigate the reaction mechanism during methane oxidation on the surface of  $\text{Co}_5\text{Mn}_1$  catalyst, we took the background in  $\text{N}_2$  atmosphere, after which we switched to the atmosphere of 1%  $\text{CH}_4 + 20\% \text{O}_2 + \text{N}_2$ , which was maintained for 30 min and then quickly switched to the atmosphere of 1%  $\text{CH}_4 + \text{Ar}$ . Elevating the reaction cell temperature to 200  $^{\circ}\text{C}$ , a rapid accumulation of key intermediate species was observed, and when  $\text{O}_2$  species in the atmosphere were removed, the accumulated key intermediate species could not be removed by complete oxidation. It is possible that it is the adsorbed oxygen species that plays the main catalytic oxidizing role at 200  $^{\circ}\text{C}$ , and the depletion of the adsorbed oxygen species leads to the loss of catalytic activity. Elevating the reaction temperature to 300  $^{\circ}\text{C}$  and repeating the

above operation, the characteristic peaks of the key intermediate species disappeared rapidly within 15 min. It is the lattice oxygen species that plays the main catalytic oxidizing role at 300  $^{\circ}\text{C}$ . At this point, the continuous oxidation of key intermediates OCHO and OCOO indicates that  $\text{CH}_4$  is oxidized mainly following the Mars-van Krevelen (MvK) mechanism.[41] Therefore, the doping of Mn leads to a significant increase in the activity of lattice oxygen in the high temperature interval.

To achieve a deep understanding of the evolution of Co, Mn and lattice oxygen ion coordinated with them in the complete oxidation of methane on  $\text{Co}_5\text{Mn}_1$  catalyst, we performed in situ studies using XPS in the temperature range of 30–400  $^{\circ}\text{C}$  by following the 1% $\text{CH}_4$ -Ar conditions. As shown in Fig. 8a, the enhancement of the satellite peak at 386.5 eV can be regarded as a sign of  $\text{Co}^{3+}$  reduction to  $\text{Co}^{2+}$ . No noticeable change of Co characteristic satellite peak was found, indicating that no  $\text{Co}^{3+}$  was reduced to  $\text{Co}^{2+}$  in the temperature range of 30–300  $^{\circ}\text{C}$ . In the temperature range of 300–400  $^{\circ}\text{C}$ , the characteristic signal of  $\text{Co}^{2+}$  appears and becomes more and more significant, indicating that  $\text{CH}_4$  reduces  $\text{Co}^{3+}$  to  $\text{Co}^{2+}$  in this temperature range.[42,43] The change of photoelectric emission spectra of Mn 3s and Mn 2p with reaction temperature reveals the transformation of Mn's combined states in the reaction (Figs. 8b and 8c). The energy difference of the multiple splitting Mn 3s spectra continues to increase from 5.0 eV to 5.5 eV with the increase in reaction temperature (30–400  $^{\circ}\text{C}$ ), indicating that the average oxidation state of Mn ions in the system decreases. In particular, the shift occurring at 250  $^{\circ}\text{C}$  compared to 30  $^{\circ}\text{C}$  is attributed to the reduction of high-valent Mn ( $\text{Mn}^{4+}$ ) ions at low temperatures. The enhancement of the acromion at around 641 eV in Mn2p results in the shift of the main peak to the direction of low binding energy, suggesting a much higher degree of electron delocalization in the reduced  $\text{Co}_5\text{Mn}_1$  with part of  $\text{Mn}^{4+}$  being reduced to  $\text{Mn}^{3+}$ . [44] Focus on the temperature at which the reduction characteristics of Co and Mn ions begin to appear, the highly valent Mn ions are more likely to interact with the reaction gas at low temperatures compared to Co ions, which verifies that the low-temperature reduction peak of  $\text{Co}_5\text{Mn}_1$  catalyst in  $\text{H}_2$  - TPR is due to the preferential reduction of Mn ions. It is also proved that the redox ability of  $\text{Mn}^{4+}$  is the critical factor to promote the complete oxidation of methane.

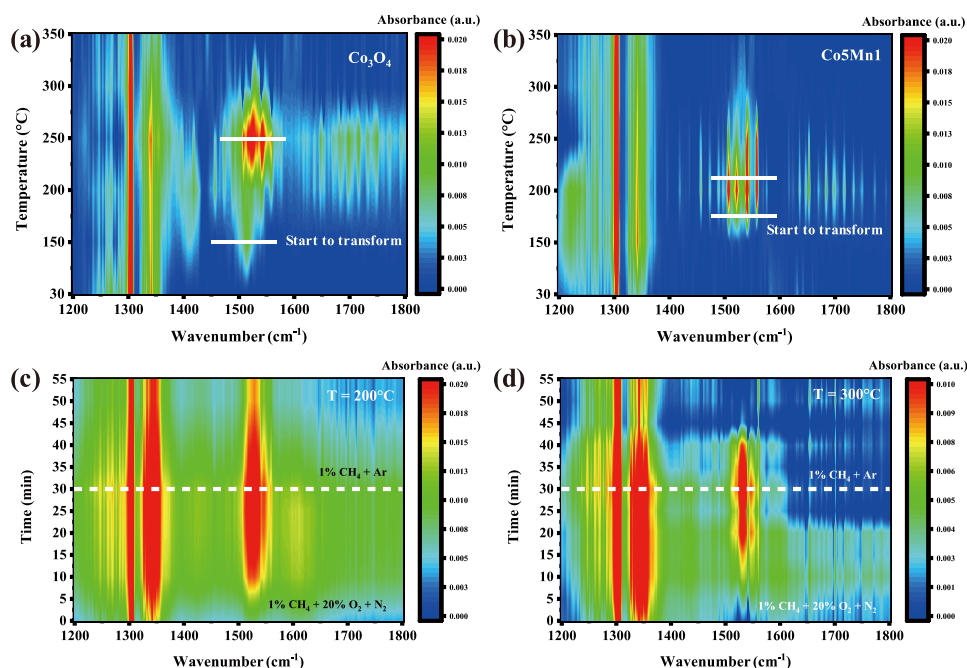


**Fig. 7.** In situ DRIFTS spectra of 1%  $\text{CH}_4$  balanced in 20% $\text{O}_2 + \text{N}_2$  gas mixture adsorption over  $\text{Co}_3\text{O}_4$  (a) and  $\text{Co}_5\text{Mn}_1$  (b) under 30–350  $^{\circ}\text{C}$ . In situ DRIFTS spectra of  $\text{Co}_5\text{Mn}_1$  samples were taken as background under  $\text{N}_2$  and switched to 1%  $\text{CH}_4 + 20\% \text{O}_2 + \text{N}_2$ , and then switched to 1%  $\text{CH}_4 + \text{Ar}$  atmospheres at 200  $^{\circ}\text{C}$  (c) and 300  $^{\circ}\text{C}$  (d).

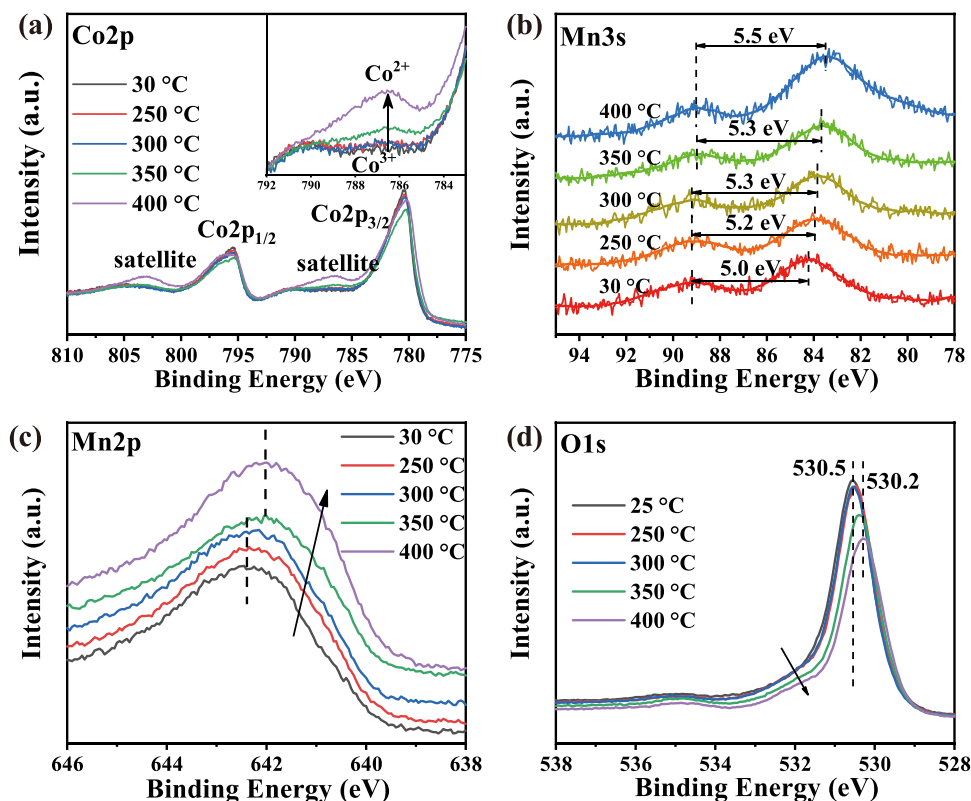


Fig. 8. In situ high-resolution XPS spectra of Co 2p (a), Mn 3s (b) and Mn 2p (c), O 1s (d) under 1%CH<sub>4</sub> + Ar gas mixture at difference temperature.

The peak of O 1s (Fig. 8d) did not shift significantly during the low-temperature reaction. The content of characteristic peaks belonging to the adsorbed oxygen species has not significantly decreased, it may be due to lack of oxygen vacancies on the surface of the Co<sub>5</sub>Mn<sub>1</sub> catalyst, thus consuming less adsorbed oxygen at low temperatures, resulting in insignificant reaction with methane in the temperature range of 30–300 °C. When the temperature was higher than 350 °C, the main peak of O 1s shifts significantly toward the low binding energy by 0.3 eV, it indicates that the surface lattice oxygen is detached from the catalyst surface causing changes in the coordination environment. Combined with the change of valence state of Mn and Co ions with temperature, the Mn ions are more easily reduced in the Mn-O-Co structure on the catalyst surface, thus inducing the surface lattice oxygen ions to participate in the reaction at a certain temperature. In order to investigate the adsorption and activation capacity of different catalysts for gaseous oxygen, we compared the  $O_{ads}/(O_{ads}+O_{latt})$  of Co<sub>3</sub>O<sub>4</sub> and Co<sub>5</sub>Mn<sub>1</sub> catalysts at different temperatures, according to the O 1s peak fitting data. As shown in Fig. S10 and Table S7, the  $O_{ads}/(O_{ads}+O_{latt})$  of Co<sub>3</sub>O<sub>4</sub> decreased from 52.35 to 19.96, a decrease of 32.39%, which is much larger than 4.73% (20.61% → 15.88%) over Co<sub>5</sub>Mn<sub>1</sub> catalyst. It was further demonstrated that the adsorption activation of pure Co<sub>3</sub>O<sub>4</sub> catalyst for gaseous oxygen was better than that of Co<sub>5</sub>Mn<sub>1</sub>.

Since it is difficult to directly observe the activation of oxygen vacancies for gaseous oxygen by in situ XPS, we tried to observe this process by O<sub>2</sub>-TPD and CH<sub>4</sub>-TPSR experiments. As shown in Fig. S11, the peak below 300 °C can be attributed to the physically adsorbed oxygen (O<sub>2(ads)</sub>) and chemically adsorbed oxygen species (O<sub>2</sub>) on the surface of the materials. The peak from 300 °C to 600 °C is generally related to the surface lattice oxygen (O<sup>2-</sup>). Fig. S11 Co<sub>3</sub>O<sub>4</sub> catalysts exhibit a higher quantity of surface chemisorbed oxygen species, suggesting that Co<sub>3</sub>O<sub>4</sub> is able to adsorb and activate more gaseous oxygen compared to Mn-doped Co<sub>3</sub>O<sub>4</sub> catalysts. The surface lattice oxygen of the Co<sub>5</sub>Mn<sub>1</sub> catalyst seems to be more easily detached from the surface, which implies

better mobility of the surface lattice oxygen of the Co<sub>5</sub>Mn<sub>1</sub> catalyst. We further conducted CH<sub>4</sub>-TPSR experiments to track CH<sub>4</sub> consumption and CO<sub>2</sub> production under different atmospheres by MS. In 1% CH<sub>4</sub> + Ar atmosphere (Fig. S12c and S12d), a CO<sub>2</sub> generation peak exists in Co<sub>3</sub>O<sub>4</sub> catalyst at around 350 °C. This is due to the fact that we have adsorbed sufficient reactive oxygen species to the intrinsic oxygen vacancies of Co<sub>3</sub>O<sub>4</sub> catalyst by air sufficiently blowing during the pretreatment process, and the reactive oxygen species are involved in the generation of CO<sub>2</sub>. In a 1% CH<sub>4</sub> + 20% O<sub>2</sub> balanced with N<sub>2</sub> (Fig. S12a and S12b), the Co<sub>5</sub>Mn<sub>1</sub> catalyst started to produce CO<sub>2</sub> at 249 °C and reached an equilibrium of CH<sub>4</sub> and CO<sub>2</sub> at 515 °C, which is much lower than that of Co<sub>3</sub>O<sub>4</sub>. Combined with the experimental results of in situ XPS, the redox of Mn-O-Co sites significantly promotes the activation of gaseous oxygen.

In addition, we recorded the spectra on the surface of different samples under the reaction atmosphere, as shown in Fig. S13, the Co2p, Mn3s, Mn2p, and O1s spectra show less variation, which is attributed to the fact that the abundance of gaseous oxygen under the reaction atmosphere is much higher than that of methane, and gaseous oxygen molecules are able to replenish the oxygen vacancies even though the oxygen vacancies are replenished.

### 3.5. Theoretical Analysis of Catalysis

DFT calculations were carried out to investigate the electronic structure of the Co<sub>x</sub>Mn<sub>y</sub> catalysts since the difference in electronic configuration may lead to alterations of the physicochemical properties. The {110} facet of pure Co<sub>3</sub>O<sub>4</sub>, and the {111} facet of Co<sub>5</sub>Mn<sub>1</sub>, which is the main exposed facet found in HAADF-STEM images (Fig. 3), are chosen to obtain surface atomic distribution. Cleave surface of the optimized conventional standard cell of Co<sub>3</sub>O<sub>4</sub> to obtain {110} facet and cleaving the standard cell of the 4Mn substitution model to obtain {111} facets. Since Co<sub>3</sub>O<sub>4</sub> {110} has two different terminations, usually denoted as the A and B terminations. The reports by Xu et al. [45] reveal

that the {110}-B surface was energetically more stable. Zasada et al.[46] conducted a comprehensive study of the structure, stability, and electronic properties of all possible terminations of the {111} surface. The stoichiometric {111}-S terminations were found to be the most stable under typical catalytic conditions. For the sake of clarity, the basic characteristics of the stoichiometric termination are depicted in Figs. 9a and 9b. Hereinafter stable  $\text{Co}_3\text{O}_4\{110\}$ -B is referred to  $\text{Co}_3\text{O}_4\{110\}$ , the stoichiometric {111}-S of  $\text{Co}_5\text{Mn}_1$  is referred to  $\text{Co}_5\text{Mn}_1\{111\}$ .

The methane molecules react with lattice oxygen to form oxygen vacancies on the surface, and then the gaseous  $\text{O}_2$  replenishes the

oxygen vacancies and regenerates lattice oxygen. Thus, the formation energy of oxygen vacancy ( $E_{\text{Ov}}$ ) and the adsorption energy ( $E_{\text{ads}}$ ) of  $\text{O}_2$  is significant for methane oxidation processing.[47,48] In Fig. 9a, there are two types of lattice oxygen for the  $\text{Co}_3\text{O}_4\{110\}$ :  $\text{O}_{2c}^{\text{I}}$  (the subscript 2c represents the coordination number) coordinates with an  $\text{Co}_{\text{Oh}}^{\text{I}}$  and an  $\text{Co}_{\text{Th}}^{\text{II}}$ ;  $\text{O}_{3c}^{\text{II}}$  coordinate with three  $\text{Co}_{\text{Oh}}^{\text{II}}$ . As shown in Fig. 9c, the calculation results verify that the  $E_{\text{Ov}}$  of 2.65 eV at the  $\text{O}_{2c}^{\text{I}}$  site is 0.36 eV lower than that at the  $\text{O}_{3c}^{\text{II}}$  site (3.01 eV). The low coordination number of  $\text{O}_{2c}^{\text{I}}$  indicates a weaker local crystal field and that it is easier to leave the surface lattice than  $\text{O}_{3c}^{\text{II}}$ . For  $\text{Co}_5\text{Mn}_1\{111\}$ , there are three types of

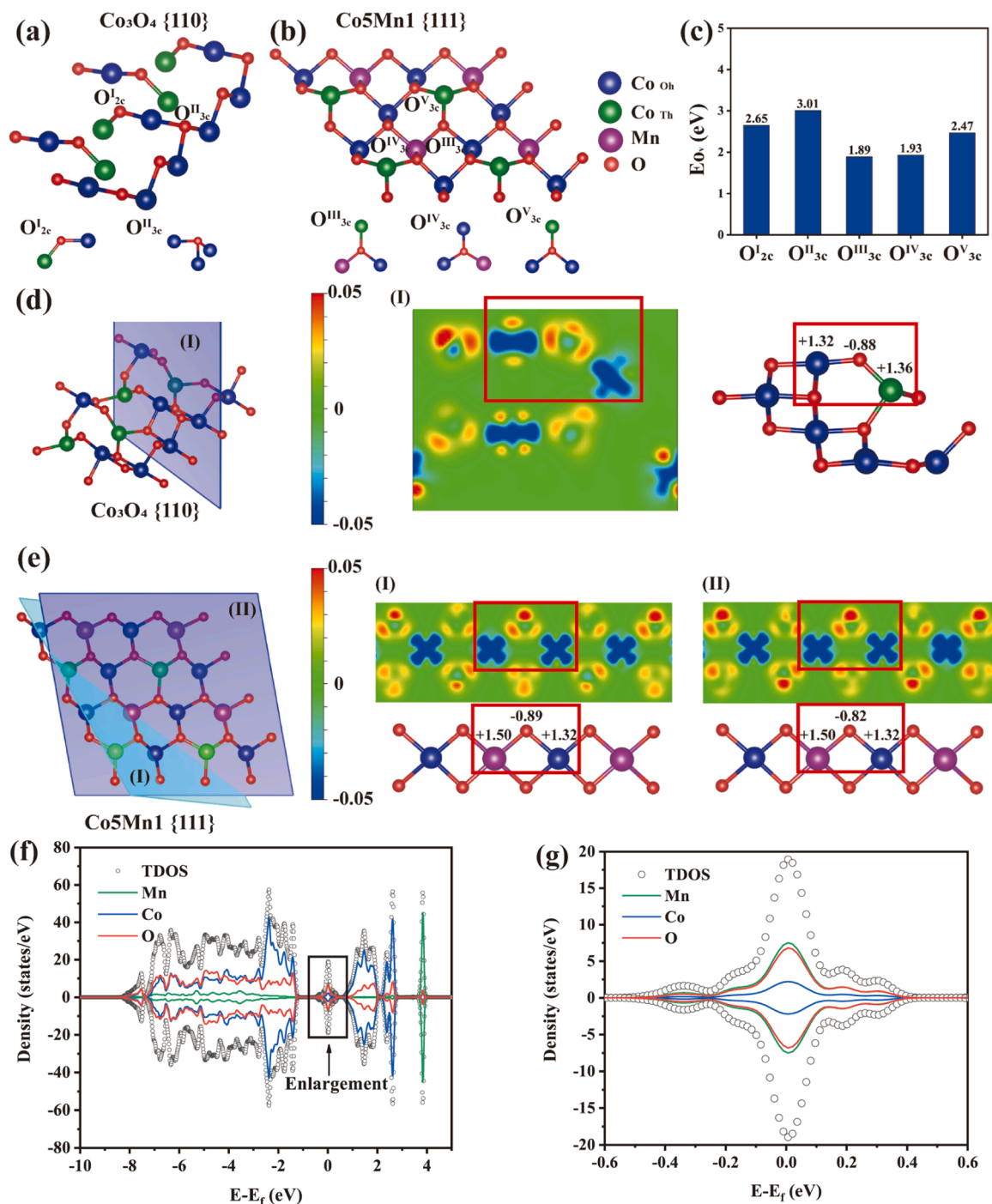


**Fig. 9.** Atomic distribution on the surface of  $\text{Co}_3\text{O}_4\{110\}$  and  $\text{Co}_5\text{Mn}_1\{111\}$ , the five exposed surface lattice oxygen ions and coordinated cations are labeled as  $\text{O}_{2c}^{\text{I}}$ ,  $\text{O}_{3c}^{\text{II}}$ ,  $\text{O}_{3c}^{\text{III}}$ ,  $\text{O}_{3c}^{\text{IV}}$  and  $\text{O}_{3c}^{\text{V}}$ , respectively (a). Oxygen vacancy generation energy ( $E_{\text{Ov}}$ ) at different sites (b). The differences in electronic transmission described by deformation charge densities diagram and the Bader charge calculation of  $\text{Co}_3\text{O}_4\{110\}$  (d) and  $\text{Co}_5\text{Mn}_1\{111\}$  (e). Density of states (DOS) for the bulk of  $\text{Co}_5\text{Mn}_1$  (f) and the enlargement near the Fermi energy level (g).

lattice oxygen (Fig. 9b):  $O_{3c}^{III}$  coordinates with a Mn, a  $Co_{Oh}$  and a  $Co_{Th}$ ;  $O_{3c}^{IV}$  coordinates with a Mn and two  $Co_{Oh}$ ;  $O_{3c}^V$  coordinates with a  $Co_{Th}$  and two  $Co_{Oh}$ . It is noteworthy that the  $E_{Ov}$  of  $O_{3c}^{IV}$  (1.93 eV) and  $O_{3c}^V$  (1.89 eV) is remarkably lower than  $O_{3c}^{III}$  (2.47 eV), revealing that  $O_{3c}$  with Mn-O-Co structure is more active as the reactive sites to be consumed in methane catalytic oxidation.

The Mn-O-Co structure may induce the activation of  $O_{3c}$  during methane oxidation. When excessive Mn substitutes the  $Co^{3+}$  site as shown in Fig. S14, the asymmetric Co-O-Mn structure transform into a symmetric Mn-O-Mn structure. The deformation charge densities diagram shows that all of Mn ion transfers fewer electrons to ortho  $O_{3c}$  in the symmetric Mn-O-Mn structure, so Mn ion presents a lower valence state. This also reveals that excessive doping of Mn leads to a decrease in the average valence state of Mn. Meanwhile, the  $E_{Ov}$  of surface lattice oxygens changes to 3.05 eV and 2.89 eV at difference site shown in Fig. S14b. The increase of  $E_{Ov}$  indicates that lattice oxygen is difficult to participate in the reaction. Further, illustrate that excessive doping of Mn ions reduces the reactivity of surface lattice oxygen.

Figs. 9d and 9e show the electron transfer during bonding in  $Co_3O_4$  {110} and the  $Co_5Mn1$  {111}, respectively. In the Co-O-Co structure, the Bader charge analysis shows that  $Co_{Th}$  and  $Co_{Oh}$  each transfer a similar number of electrons to the O ion, so the local charges are symmetrically distributed. However, in the Mn-O-Co structure constructed by Mn substitution, the Mn ion gives more electrons to bond with O (Mn-O). In particular, the Co ion gives less charge to bond with O (Co-O) based on deformation charge densities diagram and Bader charge analysis results.[49] It is known that  $Co_3O_4$  is a typical semiconductor with a band gap of about 1.5 eV.

We calculated the density of states of the Mn-doped catalysts, as shown in Fig. 9f and 9g, a new density of states feature appeared in the band gap compared to the density of states of  $Co_3O_4$ , (Fig. S15) which was attributed to the formation of stronger hybridization of Mn-3d and O-2p orbitals after Mn doping. In addition, the Mn-O-Co structure could potentially offer an enhanced electron transport pathway, which led to a more active electron transfer kinetics of  $Co_5Mn1$ , thus facilitating the participation of lattice oxygens in the reaction.

### 3.5.1. Methane molecular adsorption

The adsorption configuration of the methane molecule is shown in Fig. 10. Since the surface of  $Co_3O_4$  {110} exposes only  $Co_{Oh}^{3+}$  ions, C which exhibits electronegativity is attracted with Co ions, and one of the H is attracted by  $O_{2c}$ . For the  $Co_5Mn1$  {111} surface, the  $CH_4$  molecule prefers to adsorb to the surface delocalized  $Co_{Th}^{2+}$ . The energy calculation results show that the  $CH_4$  molecule is more readily adsorbed on the  $Co_3O_4$  {110} surface, where the adsorption energy is calculated to be  $-2.48$  eV, as compared to the optimized sites on the  $Co_5Mn1$  {111}

surface ( $-0.86$  eV). Charge density differential is one of the important tools to study the electronic structure, the yellow region implies charge aggregation, and the blue region implies charge reduction. As shown in Fig. 10b,  $CH_4$  molecule on the  $Co_3O_4$  {110} surface with  $Co_{Oh}^{3+}$  in the intermediate region where more pronounced electron aggregation occurs compared to the  $Co_5Mn1$  {111} surface, which implies that the  $Co_3O_4$  {110} surface has a stronger adsorption capacity for methane molecules.

### 3.5.2. The First C–H Bond Activation

The initial C–H bond activation serves as the pivotal step in the entire reaction process, owing to the formidable bonding energy of 435 kJ/mol associated with this chemical bond. Although the MvK mechanism of  $CH_4$  oxidation is very important, the possible pathways of the suprafacial mechanism should also be considered, the process that has been described in detail by F. Zasada et al. [41,50].

As shown in Fig. 11, C–H bond breaking could occur at the  $Co^{3+}$ ,  $O_{2c}$  or  $O_{3c}$  sites via heterolytic dissociation on the surface of  $Co_3O_4$  {110}. The adsorbed  $CH_4$  is decomposed into  $CH_3^*$  and  $H^*$  fragments, and the  $CH_3^*$  and  $H^*$  fragments stay at  $Co^{3+}$  and  $O_{2c}$  site at the transition state (TS) and final state (FS), respectively. On  $Co_5Mn1$  {111}, the exposed  $Co^{2+}$  has abundant off-domain electrons due to ligand unsaturation. Therefore,  $CH_3^*$  and  $H^*$  fragments tend to stay at  $Co^{2+}$  and  $O_{3c}$ , respectively. We conducted a comparison of their respective energy barriers and reaction energies, with the calculation results indicating that the  $Co_5Mn1$  {111} exhibits an energy barrier of 1.44 eV, which is 0.4 eV higher than that observed on  $Co_3O_4$  {110} (1.04 eV). It suggests that the  $Co^{3+}$  sites on the {110} surface have a stronger activation capacity for methane molecules, which is the main influence on the low-temperature activity of the  $Co_3O_4$  catalyst.

### 3.5.3. Oxygen molecule adsorption

In order to clarify the oxygen activation ability, optimized structure and oxygen adsorption energies were calculated over slab surface and oxygen vacancy surface of  $Co_3O_4$  {110} and  $Co_5Mn1$  {111} through the DFT method.

The adsorption of gaseous oxygen on the slab surface is shown in Fig. 12a. When oxygen molecule adsorbs at  $Co^{3+}$  site on slab surface of  $Co_3O_4$  {110}, their adsorption energies are  $-0.99$  eV, indicating that oxygen molecules on the surface of  $Co_3O_4$  {110} facilitate their adsorption and are more thermodynamically stable. When oxygen molecule adsorbs at  $Co^{2+}$  site on slab surface of  $Co_5Mn1$  {111}, the adsorption energies are  $+6.16$  eV, indicating that gaseous oxygen molecules are difficult to adsorb on the surface of  $Co_5Mn1$  {111}. The O–O bond length in the adsorbed structure of  $Co_3O_4$  {110} is elongated from 1.23 Å of gaseous oxygen to 1.32 Å, demonstrating  $Co^{3+}$  site-

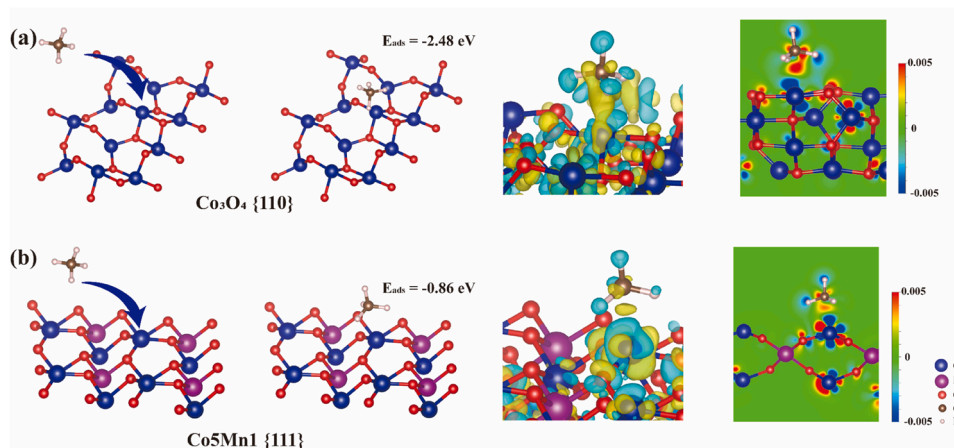


**Fig. 10.** Adsorption configurations and charge density difference diagrams of methane molecules on the  $Co_3O_4$  {110} (a) and  $Co_5Mn1$  {111} (b). Color coding: Co, blue; Mn, purple; oxygen atom, red; C, brown; H, grey.



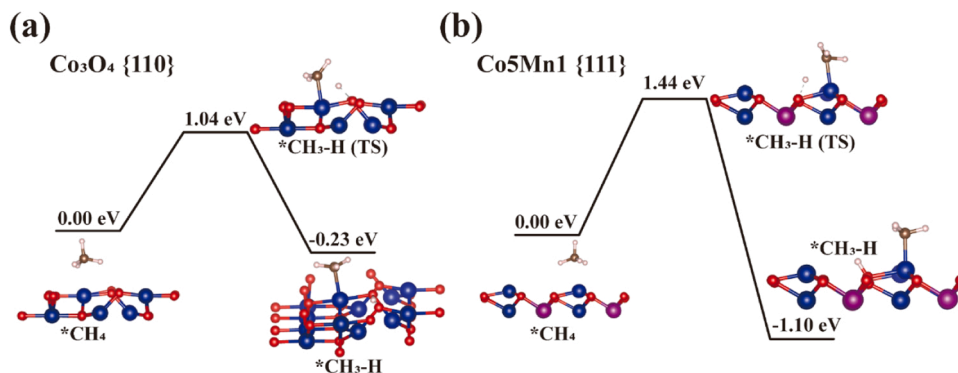


**Fig. 11.** Transition state and the final state of the first C–H activation at the exposed  $\text{Co}^{3+}$  site on  $\text{Co}_3\text{O}_4$  {110} (a), and the transition state and the final state of the first C–H activation at the exposed  $\text{Co}^{2+}$  site on  $\text{Co}_5\text{Mn1}$  {111}. Color coding: Co, blue; Mn, purple; oxygen adatom, red; C, brown; H, grey.

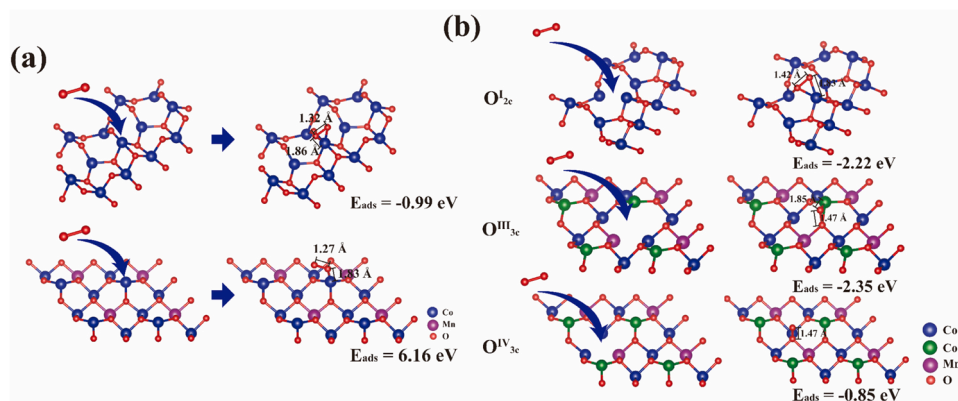


**Fig. 12.** Adsorption configurations and adsorption energy of gaseous oxygen molecules on the  $\text{Co}_3\text{O}_4$  {110} and  $\text{Co}_5\text{Mn1}$  {111} (a), adsorption configurations and adsorption energy of gaseous oxygen molecules at different defect sites on the  $\text{Co}_3\text{O}_4$  {110} and  $\text{Co}_5\text{Mn1}$  {111} (b).

induced activation of oxygen molecules. However, the O–O bond length of the oxygen molecules adsorbed on the surface of  $\text{Co}_5\text{Mn1}$  {111} remains essentially unchanged ( $1.23 \text{ \AA} \rightarrow 1.27 \text{ \AA}$ ).  $\text{O}_2$  appears to be more readily activated by adsorption on  $\text{Co}_3\text{O}_4$  {110} surfaces than on  $\text{Co}_5\text{Mn1}$  {111} surfaces at low temperatures.

Gaseous oxygen tends to adsorb to oxygen vacancies more than surface metal cations, we supplemented the calculations with the adsorption of gaseous oxygen on the oxygen vacancy surface. As shown in Fig. 12b, the oxygen molecule adsorption models were constructed at  $\text{O}_{2c}^{\text{I}}$ ,  $\text{O}_{3c}^{\text{III}}$ , and  $\text{O}_{3c}^{\text{IV}}$  sites, which are easy to generate oxygen vacancies on the surface. For  $\text{O}_{2c}^{\text{I}}$ ,  $\text{O}_{3c}^{\text{III}}$  site, one of O atom tends to recover active lattice oxygen, and other O atoms tend to bond with ortho site Co ions. In contrast, the adsorption conformation of the  $\text{O}_{3c}^{\text{IV}}$  site has one oxygen filling the oxygen vacancy while the other oxygen is present vertically without bonding to other ions. Therefore, the oxygen  $E_{\text{ads}}$  on the oxygen vacancy of  $\text{O}_{2c}^{\text{I}}$  over  $\text{Co}_3\text{O}_4$  {110} is  $-2.22 \text{ eV}$ ,  $\text{O}_{3c}^{\text{III}}$ , and  $\text{O}_{3c}^{\text{IV}}$  sites over  $\text{Co}_5\text{Mn1}$  {111} are  $-2.35 \text{ eV}$  and  $-0.85 \text{ eV}$ , respectively. The lower  $E_{\text{ads}}$  means that oxygen molecules are easily adsorbed. Therefore, the  $\text{O}_{3c}^{\text{III}}$  site on the surface of  $\text{Co}_5\text{Mn1}$  {111} is easier to adsorb activated gaseous oxygen molecules than the  $\text{O}_{2c}^{\text{I}}$  site on the surface of  $\text{Co}_3\text{O}_4$  {110}. The O–O bond distance of oxygen adsorption conformation at  $\text{O}_{2c}^{\text{I}}$ ,  $\text{O}_{3c}^{\text{III}}$ , and  $\text{O}_{3c}^{\text{IV}}$  are  $1.42 \text{ \AA}$ ,  $1.47 \text{ \AA}$  and  $1.47 \text{ \AA}$ , respectively. The elongation of the O–O bond length demonstrates that  $\text{Co}_5\text{Mn1}$  {111} has significant adsorption-induced activation of oxygen molecules. This phenomenon can be attributed to the  $\pi$ -back donation effect of the Co atoms after Mn doping, causing an enhanced electron transfer from the Co atom to the  $\pi$ -antibonding orbital of the O atom.[51] Therefore, the oxygen vacancy was facily replenished by molecular oxygen, contributing to the superior lattice oxygen activity of  $\text{Co}_5\text{Mn1}$  with respect to  $\text{Co}_3\text{O}_4$ .

In this chapter, we compared the oxygen vacancy generation energy ( $E_{\text{OV}}$ ), activation energy of methane molecules, adsorption energy ( $E_{\text{ads}}$ ) of methane molecules on slab surface, and adsorption energy of oxygen molecules on slab surface and defective surface on the different site of  $\text{Co}_3\text{O}_4$  {110} and  $\text{Co}_5\text{Mn1}$  {111}. It is noteworthy that the  $\text{Co}_3\text{O}_4$  {110} slab is more favorable for the activation of methane molecules and gaseous oxygen molecules. However, the constructed Mn–O–Co structure over  $\text{Co}_5\text{Mn1}$  {111} can effectively optimize the electronic structure and significantly reduce the oxygen vacancy generation energy than Co–O–Co structure over  $\text{Co}_3\text{O}_4$  {110}, making it easier for the surface lattice oxygen participates in the reaction. In addition, the oxygen vacancies generated are more powerful for the adsorption and activation of gaseous oxygen. Some studies have demonstrated that high temperatures promote the production of oxygen vacancies. Since  $\text{Co}_3\text{O}_4$  catalysts have more abundant intrinsic oxygen vacancies compared to  $\text{Co}_5\text{Mn1}$  catalysts, the promotion of oxygen vacancies for gaseous oxygen activation at low temperatures should not be neglected, and the synergistic surface  $\text{Co}_{\text{OH}}^{3+}$  for gaseous oxygen activation contributes to the good methane catalytic efficiency of  $\text{Co}_3\text{O}_4$  catalysts at low temperatures.

The absence of intrinsic oxygen vacancies in the  $\text{Co}_5\text{Mn1}$  catalyst due to the doping of high-valent Mn ions limits the activation of oxygen vacancies for gaseous oxygen at low temperatures. Although the oxygen vacancies in  $\text{Co}_5\text{Mn1}$  {111} are more favorable for the adsorption and activation of gaseous oxygen. Meanwhile  $\text{Co}_5\text{Mn1}$  {111} is difficult to adsorb gaseous oxygen directly ( $E_{\text{ads}}=6.16 \text{ eV}$ ). Therefore, the low-temperature catalytic activity of  $\text{Co}_5\text{Mn1}$  is lower than  $\text{Co}_3\text{O}_4$ . However, the surface lattice oxygen coordinated with Mn and Co ions has a lower oxygen vacancy generation energy, so an increase in temperature can induce more oxygen vacancy generation compared to pure  $\text{Co}_3\text{O}_4$ . The increase in oxygen vacancies in turn promotes the activation of

gaseous oxygen on the surface because of the low gaseous oxygen adsorption energy of Co<sub>5</sub>Mn<sub>1</sub> {111}. The gaseous oxygen activated by oxygen vacancy adsorption may be a key factor in promoting methane reactions at high temperatures. The positive feedback mechanism starts with the high temperature effect promoting the generation of oxygen vacancies. This is the reason why Co<sub>5</sub>Mn<sub>1</sub> catalyst has higher catalytic efficiency than Co<sub>3</sub>O<sub>4</sub> catalyst in the high temperature range. In summary, the adsorption and activation of intrinsic oxygen vacancies on the surface of Co<sub>3</sub>O<sub>4</sub> {110} for gaseous oxygen dominate the low-temperature catalytic activity. The induced oxygen vacancies generated by Mn-O-Co on the Co<sub>5</sub>Mn<sub>1</sub> {111} dominate the high-temperature catalytic activity.

#### 4. Conclusion

In conclusion, a series of Mn-substituted Co<sub>3</sub>O<sub>4</sub> catalysts were prepared by the oxalic acid synchronous complexation method for the complete oxidation of methane. Mn ions were successfully incorporated into the lattice of Co<sub>3</sub>O<sub>4</sub> in high dispersion. Structural and theoretical analysis reveals that the appropriate amount of Mn ions substituted Co<sub>3</sub>O<sub>4</sub> sites construct the Mn-O-Co structure. Since Mn exists mainly in the high valence state, more lattice oxygen ions are needed to balance the charge. Therefore, the intrinsic oxygen vacancies concentration decreases with the increase of Mn doping. To distinguish from intrinsic oxygen vacancies, we define induced oxygen vacancies as oxygen vacancies generated by changes in reaction atmosphere and temperature and design experiments to investigate the evolution of both in the reaction and the mechanism of action.

The results of in situ DRIFTS, in situ XPS, and DFT revealed that the pure Co<sub>3</sub>O<sub>4</sub> catalyst exhibited good catalytic activity at low temperature due to its abundant intrinsic oxygen vacancies, which induced the activation of adsorbed gaseous oxygen, promoting the conversion of methane at low temperatures. The outstanding high-temperature catalytic activity of the Co<sub>5</sub>Mn<sub>1</sub> catalyst is attributed to the asymmetrical Mn-O-Co structure constructed by Mn substituting, where Mn transfers more electrons to coordinated oxygen and inhibits electron transfer from Co ions to coordinated oxygen, which is significantly reduces the oxygen vacancy formation energy. Thus, surface lattice oxygen is promoted to participate more readily in methane oxidation reactions at high temperatures. Generated Mn-O<sub>v</sub>-Co sites more tend to adsorb activated gaseous oxygen compared to the Co-O<sub>v</sub>-Co sites, thus increasing the catalyst surface oxygen cycling rate. In conclusion, the intrinsic oxygen vacancy in the low-temperature region dominates the adsorption activation of gaseous oxygen, while the induced oxygen vacancy table dominates the high-temperature region, which is the main mechanism by which Mn doping increases the catalyst activity for complete methane oxidation.

#### CRedit authorship contribution statement

**Linghe Song:** Methodology Validation Writing – original draft, **Hang Zhang:** Validation, **Juxia Xiong:** Methodology, **Ziyang Chen:** Investigation, **Yue Liu:** Data Curation, **Haitao Zhou:** Resources, **Weixing Yang:** Investigation, **Dahua Cao:** Data curation, **Haomin Huang:** Writing – review & editing, **Limin Chen:** Project administration, **Mingli Fu:** Supervision, **Daiqi Ye:** Funding acquisition.

#### Declaration of Competing Interest

The authors report no declarations of interest.

#### Data Availability

Data will be made available on request.

#### Acknowledgment

The work was supported by the Guangdong Basic and Applied Basic Research Foundation [No. 2021A1515011378], National Natural Science Foundation of China [No. 51878292].

#### Notes

The authors declare no competing financial interest.

#### Appendix A. Supporting information

Supplementary data associated with this article can be found in the online version at doi:10.1016/j.apcatb.2023.123547.

#### References

- [1] R.B. Jackson, M. Saunio, P. Bousquet, J.G. Canadell, B. Poulter, A.R. Stavert, P. Bergamaschi, Y. Niwa, A. Segers, A. Tsuruta, Increasing anthropogenic methane emissions arise equally from agricultural and fossil fuel sources, *Environ. Res. Lett.* 15 (2020), 071002.
- [2] IPCC Sixth Assessment Report: Climate Change, (2021).
- [3] J.H. Lee, D.L. Trimm, Catalytic combustion of methane, *Fuel Process. Technol.* 42 (1995) 339–359.
- [4] T.V. Choudhary, S. Banerjee, V.R. Choudhary, Catalysts for combustion of methane and lower alkanes, *Appl. Catal. A: Gen.* 234 (2002) 1–23.
- [5] J. Xiong, J. Yang, X. Chi, K. Wu, L. Song, T. Li, Y. Zhao, H. Huang, P. Chen, J. Wu, L. Chen, M. Fu, D. Ye, Pd-Promoted Co<sub>2</sub>NiO<sub>4</sub> with lattice Co-O-Ni and interfacial Pd-O activation for highly efficient methane oxidation, *Appl. Catal. B: Environ.* 292 (2021), 120201.
- [6] Y. Cai, J. Xu, Y. Guo, J. Liu, Ultrathin, polycrystalline, two-dimensional Co<sub>3</sub>O<sub>4</sub> for low-temperature CO oxidation, *ACS Catal.* 9 (2019) 2558–2567.
- [7] Q. Yu, C. Liu, X. Li, C. Wang, X. Wang, H. Cao, M. Zhao, G. Wu, W. Su, T. Ma, J. Zhang, H. Bao, J. Wang, B. Ding, M. He, Y. Yamauchi, X.S. Zhao, N. -doping Act. Defect. Co<sub>3</sub>O<sub>4</sub> Effic. Catal. Low. -Temp. methane Oxid., *Appl. Catal. B: Environ.* 269 (2020), 118757.
- [8] Y. Li, T. Chen, S. Zhao, P. Wu, Y. Chong, A. Li, Y. Zhao, G. Chen, X. Jin, Y. Qiu, D. Ye, Engineering cobalt oxide with coexisting cobalt defects and oxygen vacancies for enhanced catalytic oxidation of toluene, *ACS Catal.* (2022) 4906–4917.
- [9] W. Zhang, K. Lassen, C. Descorme, J.L. Valverde, A. Giroir-Fendler, Effect of the precipitation pH on the characteristics and performance of Co<sub>3</sub>O<sub>4</sub> catalysts in the total oxidation of toluene and propane, *Appl. Catal. B: Environ.* 282 (2021), 119566.
- [10] P. Losch, W. Huang, O. Vozniuk, E.D. Goodman, W. Schmidt, M. Cargnello, Modular Pd/Zelite Composites Demonstrating the Key Role of Support Hydrophobic/Hydrophilic Character in Methane Catalytic Combustion, *ACS Catal.* 9 (2019) 4742–4753.
- [11] Y. Ma, L. Wang, J. Ma, H. Wang, C. Zhang, H. Deng, H. He, Investigation into the enhanced catalytic oxidation of o-xylene over mof-derived Co<sub>3</sub>O<sub>4</sub> with different shapes: the role of surface twofold-coordinate lattice oxygen (O<sub>2</sub>), *ACS, Catalysis* 11 (2021) 6614–6625.
- [12] C. Dong, Z. Qu, Y. Qin, Q. Fu, H. Sun, X. Duan, Revealing the highly catalytic performance of spinel CoMn<sub>2</sub>O<sub>4</sub> for toluene oxidation: involvement and replenishment of oxygen species using in situ designed-tp techniques, *ACS, Catalysis* 9 (2019) 6698–6710.
- [13] T. Wang, Y. Sun, Y. Zhou, S. Sun, X. Hu, Y. Dai, S. Xi, Y. Du, Y. Yang, Z.J. Xu, Identifying influential parameters of octahedrally coordinated cations in spinel ZnMn<sub>x</sub>Co<sub>2-x</sub>O<sub>4</sub> oxides for the oxidation reaction, *ACS Catal.* 8 (2018) 8568–8577.
- [14] F.F. Tao, J.J. Shan, L. Nguyen, Z. Wang, S. Zhang, L. Zhang, Z. Wu, W. Huang, S. Zeng, P. Hu, Understanding complete oxidation of methane on spinel oxides at a molecular level, *Nat. Commun.* 6 (2015) 7798.
- [15] J. Bae, D. Shin, H. Jeong, C. Choe, Y. Choi, J.W. Han, H. Lee, Facet-dependent Mn Doping on shaped Co<sub>3</sub>O<sub>4</sub> crystals for catalytic oxidation, *ACS Catalysis* 11 (2021) 11066–11074.
- [16] K. Papadatos, K.A. Shelstad, Catalyst screening using a stone DTA apparatus: I. Oxidation of toluene over cobalt-metal-oxide catalysts, *J. Catal.* 28 (1973) 116–123.
- [17] H. Baussart, R. Delobel, M. Le Bras, J.M. Leroy, Oxidation of propene on mixed oxides of copper and cobalt, *J. Chem. Soc. Faraday Trans. 1: Phys. Chem. Condens. Phases* 75 (1979) 1337–1345.
- [18] F. Zasada, W. Piskorz, J. Janas, J. Gryboś, P. Indyka, Z. Sojka, Reactive oxygen species on the (100) facet of cobalt spinel nanocatalyst and their relevance in 16o2/18o2 isotopic exchange, den2o, and dech4 processes—a theoretical and experimental account, *ACS Catal.* 5 (2015) 6879–6892.
- [19] J. Li, X. Liang, S. Xu, J. Hao, Catalytic performance of manganese cobalt oxides on methane combustion at low temperature, *Appl. Catal. B: Environ.* 90 (2009) 307–312.
- [20] Y. Zheng, Y. Yu, H. Zhou, W. Huang, Z. Pu, Combustion of lean methane over Co<sub>3</sub>O<sub>4</sub> catalysts prepared with different cobalt precursors, *RSC Adv.* 10 (2020) 4490–4498.

- [21] P. Liu, Y. Liao, J. Li, L. Chen, M. Fu, P. Wu, R. Zhu, X. Liang, T. Wu, D. Ye, Insight into the effect of manganese substitution on mesoporous hollow spinel cobalt oxides for catalytic oxidation of toluene, *J. Colloid Interface Sci.* 594 (2021) 713–726.
- [22] A. Navrotsky, O.J. Kleppa, The thermodynamics of cation distributions in simple spinels, *J. Inorg. Nucl. Chem.* 29 (1967) 2701–2714.
- [23] S. Zhao, T. Li, J. Lin, P. Wu, Y. Li, A. Li, T. Chen, Y. Zhao, G. Chen, L. Yang, Y. Meng, X. Jin, Y. Qiu, D. Ye, Engineering  $\text{Co}^{3+}$ -rich crystal planes on  $\text{Co}_3\text{O}_4$  hexagonal nanosheets for CO and hydrocarbons oxidation with enhanced catalytic activity and water resistance, *Chem. Eng. J.* 420 (2021), 130448.
- [24] Q. Ke, D. Yi, Y. Jin, F. Lu, B. Zhou, F. Zhan, Y. Yang, D. Gao, P. Yan, C. Wan, P. Cui, D. Golberg, J. Yao, X. Wang, Manganese doping in cobalt oxide nanorods promotes catalytic dehydrogenation, *ACS Sustain. Chem. Eng.* 8 (2020) 5734–5741.
- [25] R.D. Shannon, Revised effective ionic radii and systematic studies of interatomic distances in halides and chalcogenides, *Acta Crystallogr. Sect. A*, A32 (1976) 751.
- [26] T. Hirata, Oxygen position, octahedral distortion, and bond-valence parameter from bond lengths in  $\text{Ti}_{1-x}\text{Sn}_x\text{O}_2$  ( $0 \leq x \leq 1$ ), *J. Am. Ceram. Soc.* 83 (2000) 3205–3207.
- [27] C.M. Julien, M. Massot, C. Poinssignon, Lattice vibrations of manganese oxides, *Spectrochim. Acta Part A: Mol. Biomol. Spectrosc.* 60 (2004) 689–700.
- [28] J. Zuo, C. Xu, Y. Liu, Y. Qian, Crystallite size effects on the Raman spectra of  $\text{Mn}_3\text{O}_4$ , *Nanostruct. Mater.* 10 (1998) 1331–1335.
- [29] Q. Ren, S. Mo, R. Peng, Z. Feng, M. Zhang, L. Chen, M. Fu, J. Wu, D. Ye, Controllable synthesis of 3D hierarchical  $\text{Co}_3\text{O}_4$  nanocatalysts with various morphologies for the catalytic oxidation of toluene, *J. Mater. Chem. A* 6 (2018) 498–509.
- [30] W. Zhang, M. Li, X. Wang, X. Zhang, X. Niu, Y. Zhu, Boosting catalytic toluene combustion over Mn doped  $\text{Co}_3\text{O}_4$  spinel catalysts: Improved mobility of surface oxygen due to formation of Mn-O-Co bonds, *Appl. Surf. Sci.* 590 (2022), 153140.
- [31] S. Mo, Q. Zhang, J. Li, Y. Sun, Q. Ren, S. Zou, Q. Zhang, J. Lu, M. Fu, D. Mo, J. Wu, H. Huang, D. Ye, Highly Effic. Mesoporous  $\text{MnO}_2$  Catal. Total toluene Oxid.: Oxyg.-Vacancy Defect Eng. Invol. Intermed. Using situ DRIFTS, *Appl. Catal. B: Environ.* 264 (2020).
- [32] I. Nakamura, N. Negishi, S. Kutsuna, T. Ihara, S. Sugihara, K. Takeuchi, Role of oxygen vacancy in the plasma-treated  $\text{TiO}_2$  photocatalyst with visible light activity for NO removal, *J. Mol. Catal. A: Chem.* 161 (2000) 205–212.
- [33] G. Zhu, H. Yang, Y. Jiang, Z. Sun, X. Li, J. Yang, H. Wang, R. Zou, W. Jiang, P. Qiu, W. Luo, Modulating the electronic structure of FeCo nanoparticles in n-doped mesoporous carbon for efficient oxygen reduction reaction, *Adv. Sci. (Weinh.)* (2022) e2200394.
- [34] J. Yang, H. Liu, W.N. Martens, R.L. Frost, Synthesis and characterization of cobalt hydroxide, cobalt oxyhydroxide, and cobalt oxide nanodiscs, *J. Phys. Chem. C* 114 (2010) 111–119.
- [35] V.P. Santos, O.S.G.P. Soares, J.J.W. Bakker, M.F.R. Pereira, J.J.M. Órfão, J. Gascon, F. Kapteijn, J.L. Figueiredo, Structural and chemical disorder of cryptomelane promoted by alkali doping: Influence on catalytic properties, *J. Catal.* 293 (2012) 165–174.
- [36] M. Sun, B. Lan, T. Lin, G. Cheng, F. Ye, L. Yu, X. Cheng, X. Zheng, Controlled synthesis of nanostructured manganese oxide: crystalline evolution and catalytic activities, *CrystEngComm* 15 (2013).
- [37] G. Mitran, S. Chen, D.-K. Seo, Role of oxygen vacancies and  $\text{Mn}^{4+}/\text{Mn}^{3+}$  ratio in oxidation and dry reforming over cobalt-manganese spinel oxides, *Mol. Catal.* 483 (2020).
- [38] Y. Shen, J. Deng, S. Impeng, S. Li, T. Yan, J. Zhang, L. Shi, D. Zhang, Boosting toluene combustion by engineering co-o strength in cobalt oxide catalysts, *Environ. Sci. Technol.* 54 (2020) 10342–10350.
- [39] F. Liu, H. He, Y. Ding, C. Zhang, Eff. Manganese Substit. Struct. Act. iron Titan. Catal. Sel. Catal. Reduct. NO  $\text{NH}_3$ , *Appl. Catal. B: Environ.* 93 (2009) 194–204.
- [40] Y. Zhang, J. Zhu, S. Li, Y. Xiao, Y. Zhan, X. Wang, C.-t. Au, L. Jiang, , Rational design of highly  $\text{H}_2\text{O}$ - and  $\text{CO}_2$ -tolerant hydroxyapatite-supported Pd catalyst for low-temperature methane combustion, *Chem. Eng. J.* 396 (2020), 125225.
- [41] F. Zasada, J. Janas, W. Piskorz, M. Gorczyńska, Z. Sojka, Total oxidation of lean methane over cobalt spinel nanocubes controlled by the self-adjusted redox state of the catalyst: experimental and theoretical account for interplay between the langmuir-hinshelwood and mars-van krevelen mechanisms, *ACS Catal.* 7 (2017) 2853–2867.
- [42] L. Lukashuk, N. Yigit, R. Rameshan, E. Kolar, D. Teschner, M. Havecker, A. Knop-Gericke, R. Schlögl, K. Föttinger, G. Rupprechter, Operando insights into co oxidation on cobalt oxide catalysts by NAP-XPS, FTIR, and XRD, *ACS Catal.* 8 (2018) 8630–8641.
- [43] L. Song, J. Xiong, H. Cheng, J. Lu, P. Liu, M. Fu, J. Wu, L. Chen, H. Huang, D. Ye, In-Situ characterizations to investigate the nature of  $\text{Co}^{3+}$  coordination environment to activate surface adsorbed oxygen for methane oxidation, *Appl. Surf. Sci.* 556 (2021), 149713.
- [44] L. Chen, J. Zhang, J. Wang, P. Chen, M. Fu, J. Wu, D. Ye, Insight into the improvement effect of nitrogen dopant in ag/co3o4 nanocubes for soot oxidation: experimental and theoretical studies, *J. Hazard Mater.* 420 (2021), 126604.
- [45] X.-L. Xu, Z.-H. Chen, Y. Li, W.-K. Chen, J.-Q. Li, Bulk and surface properties of spinel  $\text{Co}_3\text{O}_4$  by density functional calculations, *Surf. Sci.* 603 (2009) 653–658.
- [46] F. Zasada, J. Gryboś, W. Piskorz, Z. Sojka, Cobalt Spinel (111) facets of various stoichiometry—DFT+U and Ab initio thermodynamic investigations, *J. Phys. Chem. C* 122 (2018) 2866–2879.
- [47] J. Paier, C. Penschke, J. Sauer, Oxygen defects and surface chemistry of ceria: quantum chemical studies compared to experiment, *Chem. Rev.* 113 (2013) 3949–3985.
- [48] Z. Li, Q. Yan, Q. Jiang, Y. Gao, T. Xue, R. Li, Y. Liu, Q. Wang, Oxygen vacancy mediated  $\text{Cu}_y\text{Co}_{3-y}\text{Fe}_1\text{O}_8$  mixed oxide as highly active and stable toluene oxidation catalyst by multiple phase interfaces formation and metal doping effect, *Appl. Catal. B: Environ.* 269 (2020).
- [49] A. Li, S. Kong, C. Guo, H. Ooka, K. Adachi, D. Hashizume, Q. Jiang, H. Han, J. Xiao, R. Nakamura, Enhancing the stability of cobalt spinel oxide towards sustainable oxygen evolution in acid, *Nat. Catal.* 5 (2022) 109–118.
- [50] F. Zasada, J. Gryboś, C. Hudy, J. Janas, Z. Sojka, Total oxidation of lean methane over cobalt spinel nanocubes—mechanistic vistas gained from DFT modeling and catalytic isotopic investigations, *Catal. Today* 354 (2020) 183–195.
- [51] L. Xu, Y. Zou, Z. Xiao, S. Wang, Transforming  $\text{Co}_3\text{O}_4$  nanosheets into porous N-doped Co O nanosheets with oxygen vacancies for the oxygen evolution reaction, *J. Energy Chem.* 35 (2019) 24–29.